Intra-cluster receptor density (IRD) dictates TNFR1 clusters' signaling efficacy

Subhamoy Jana[1#], Priyanka Roy[1#], Jibitesh Das[2], Parijat Biswas[1], Nandana Nanda[1], Bidisha Sinha[2], Deepak Kumar Sinha[1*]

[1] School of Biological Sciences, Indian Association for the Cultivation of Science, Kolkata 700032, India.

[2] Department of Biological Sciences, Indian Institute of Science Education and Research Kolkata, Nadia, Mohanpur 741246, India.

[#] Equal first-author contribution

* Corresponding author: Deepak Kumar Sinha
Email: bcdks@iacs.res.in, emaildks@gmail.com

Abstract

Tumor Necrosis Factor Receptor 1 (TNFR1) signaling determines cell fate during inflammation, immunopathogenesis, and tumorigenesis. TNFR1 proteins homo-oligomerize into clusters on the plasma membrane. The potential impact of TNFR1 clustering on downstream signaling remains unexplored. Homo-FRET measurements elucidate that alterations in intra-cluster receptor density (IRD) dictate the outcomes of downstream TNFR1 signaling. Soluble TNF-α (sTNF-α) elevates IRD within the TNFR1 clusters' core while diminishing it in the rim, through intra-cluster dynamic reorganization of TNFR1. Decreasing TNFR1 IRD through increasing membrane tension, administering TNFR1 antagonist zafirlukast, actin depolymerization, or depleting cholesterol impedes sTNF-α-mediated stimulation. Conversely, increasing IRD by reducing membrane tension or exposing cells to 3D gel-like microenvironment induces ligand-independent TNFR1 signaling. These findings suggest a broader applicability of IRD in modulating signaling pathways across other receptor families, offering insights for innovative strategies in TNFR1 signaling modulation.

MAIN TEXT

Introduction

Tumor necrosis factor receptor 1 (TNFR1) is a type I transmembrane protein of the TNF receptor superfamily (TNFRSF) (*1*, *2*), which plays a multifaceted role in modulating numerous cellular processes, encompassing inflammation (*3*, *4*), cell survival (*5*), apoptosis (*6*, *7*), and differentiation (*8*). While TNF-α-mediated TNFR1 signaling pathways are widely known (*9*, *10*), the role of receptor clustering in downstream signal activation remains unexplored. Studies in cell-free systems suggest that the trimeric ligand TNF-α (*11*) interacts with TNFR1s in their native monomeric and/or dimeric state (*12*) to form the trimeric TNFR1 primary cluster (*13*), which acts as the basic signaling unit. Further, the interaction among pre-ligand assembly domains (PLAD) across different TNFR1 primary clusters promotes the formation of ligand-independent, higher-order TNFR1 secondary clusters on the cell membrane (*14*–*18*). Besides PLAD, TNFR1 interacts via its other domains, including cysteine-rich domains (CRDs) (*19*), transmembrane domain (TMD) (*20*), and cytoplasmic domain (CD) (*21*, *22*), assembling ligand-receptor and receptor-receptor complexes into larger clusters. Our observation, along with others (*18*, *21*), indicates that TNFR1 consistently forms pre-formed clusters on the cell membrane even without additional ligand stimulation.

Understanding the importance of TNFR1 clustering in downstream signaling is crucial for therapeutic advancements. Current targeted treatments for polymorphism-induced TNFR1 dysfunctions (*23*–*28*) are limited, primarily focusing on ligand sequestration or decoy receptors (*29*). Thus, it highlights the need for a deeper understanding of TNFR1 cluster organization and its role in modulating downstream signaling across various conditions.

TNFR1 clustering has been studied with its ligand at basal and stimulated states (*14*), but the organization within pre-formed clusters and their impact on downstream signaling remain unclear. A previous study on TNFR1 signal activation by reinforcing secondary clusters with agonistic antibodies (*30*, *31*) suggests that an increase in receptor density within the cluster activates the signaling. In our study, we showed that the density of TNFR1 receptors within pre-formed TNFR1 clusters, referred to as intra-cluster receptor density (IRD), is a crucial determinant of its downstream signaling. We anticipated that IRD modulates signaling efficacy through cooperativity, which refers to the proximity of receptors within a cluster.

Manipulating the IRD while preserving other biochemical elements is a challenging task. Using HeLa as a model system, we subjected cells to diverse conditions that alter TNFR1 cluster's IRD to examine its link with the TNFR1 downstream signaling state. Initially, we investigated if activation and inhibition of TNFR1 signaling by soluble TNF-α (sTNF-α) (*32*) and antagonist zafirlukast (*33*) respectively, occurs by modulating the IRD. Further, we explored the impact of altered plasma membrane tension, actin depolymerization, changes in extracellular microenvironment, and cholesterol depletion on TNFR1's IRD and signaling efficacy. Subsequently, we monitored the IRD of TNFR1-EGFP clusters expressed in HeLa cells using homo-FRET, measured by the reduction in fluorescence anisotropy (*34–36*). Variations in fluorescence anisotropy within TNFR1-EGFP clusters indicate differential homo-FRET efficiency, where the anisotropy map inversely correlates with the TNFR1 IRD. TNFR1 signal activation triggers IKK phosphorylation leading to NF-κB (p65/p50) nuclear translocation (*37*). We assessed the downstream signaling of TNFR1 by NF-κB activation assay in different physiological conditions which can alter the TNFR1 IRD.

This manuscript demonstrates that altering the TNFR1 IRD changes the response to TNF-α in downstream signaling, both in a ligand-dependent and ligand-independent manner. Our findings provide valuable insights into the role of clustering in TNFRSF function and its potential implications for therapeutic strategies.

Results

Homo-FRET mapping of TNFR1-EGFP clusters reveals heterogeneous IRD in HeLa cells

We cloned the human TNFR1 protein in the mEGFP-N1 backbone to generate TNFR1-EGFP construct (**Fig. 1a**). Immunostaining of TNFR1 in transiently transfected HeLa cells revealed that the chimeric TNFR1-EGFP molecules assemble into small clusters on the membrane, like endogenous TNFR1. We designated clusters devoid of EGFP as "endogenous" and those with EGFP as "exogenous" (**Fig. 1b, S1a**). The colocalization of EGFP and anti-TNFR1 (**Fig. 1b**), and the sequencing data (**Supplementary document 1**) confirmed the structural and sequence accuracy of the chimeric protein. The fraction of TNFR1-EGFP clusters on the plasma membrane increased with time after transfection (**Fig. S1b**), reaching up to 76 ± 8% in 18 hours (**Fig. 1c, Supplementary video 1**). A small fraction of TNFR1-EGFP clusters exhibited higher mobility (**Supplementary video 2**), presumably due to its localization on intracellular vesicles. **Fig. S1b** confirmed that most of the investigated TNFR1-EGFP clusters were on the plasma membrane.

The fluorescence anisotropy (r) map of TNFR1-EGFP clusters in live cells (**Fig. 1d**) displayed notable intra-cluster variations of r values (**Fig. 1d-iv**). In most clusters, the central core (**Fig. 1d-iv, 1e**) revealed lower anisotropy (r_{core}) compared to the surrounding rim's anisotropy (r_{rim}), suggesting that the intra-cluster variations in r originated from varying homo-FRET efficiencies within the cluster (**Fig. S1c**). The lower r_{core} value implied a heightened homo-FRET efficiency in the core, indicating a denser packing of TNFR1 molecules in the core than in the rim or a higher IRD in the core than the rim.

To validate our hypothesis, we investigated the impact of photobleaching on the r map of the cluster. Following photobleaching of the TNFR1-EGFP cluster, we observed a decline in homo-FRET efficiency, which was indicated by an increase in anisotropy (**Fig. S1c, S1d**) (*36, 38*). Moreover, we anticipated a larger rise in anisotropy within the core compared to the rim post-photobleaching. **Fig. 1f** suggested that intra-cluster variations in mean anisotropy of the core ($\bar{r}_{core}$) and the rim ($\bar{r}_{rim}$) were due to differing homo-FRET efficiencies. Notably, a uniform anisotropy map was observed when the cluster was photobleached to the extent of negligible homo-FRET in both the core and rim (**Fig. S1e**). This uniformity suggested that the anisotropy pattern in **Fig. 1d-iv** was not due to imaging or computational artifacts.

Using siRNA to deplete TNFR1, next we examined the influence of TNFR1 expression levels on IRD in HeLa cells (**Fig. 1g**). Downregulation of endogenous TNFR1 reduced the area of both endogenous and exogenous clusters (**Fig. 1h**). Notably, the reduction in area of endogenous clusters in TNFR1-EGFP transfected cells was less pronounced (**Fig. 1h**). The average areas of both endogenous and exogenous clusters were statistically comparable (**Fig. S1f**), however in overexpressed condition, we observed a few clusters whose areas exceeded those of the largest clusters in control condition. Comparing $\bar{r}_{core}$ and $\bar{r}_{rim}$ of TNFR1-EGFP in control cells to TNFR1-depleted cells (**Fig. 1i**) revealed that TNFR1 depletion did not affect cluster IRD. Furthermore, $\bar{r}_{core}$ and $\bar{r}_{rim}$ remained independent of the cluster's area (**Fig. S1g**).

The intra-cluster receptor molecules undergo continuous reorganization

We examined the intra-cluster dynamics of TNFR1 molecules under physiological conditions. Time-lapse anisotropy maps of TNFR1-EGFP clusters in live HeLa cells (**Fig. 2a**) revealed significant temporal variations in r_{core}. In contrast, we observed a significantly smaller temporal variation of r_{core}

over 90-second duration in fixed cells (**Fig. 2b**). It remained uncertain whether the greater temporal variations of r_{core} in live cells result from dynamic changes in local IRD within the core or if they represent measurement noise. To address this uncertainty, we compared the changes in the cluster's $\bar{r}_{core}$ in live cells with those in fixed cells (**Fig. 2c-d**). We hypothesized that the crosslinking of proteins hinders the intra-cluster reorganization of TNFR1-EGFP molecules. The notably lower variations (±5%) of $\bar{r}_{core}$ in fixed clusters compared to live clusters (±20%) indicated that the temporal variations of $\bar{r}_{core}$ in live cells originated from a change in the local IRD due to intra-cluster reorganization of receptors. **Fig. 2d** further suggested that the anisotropy changes exceeding 5% in our experimental setup signify a genuine change in IRD, given a negligible change in the total number of receptors within the cluster. The fluorescence recovery after photobleaching (FRAP) investigation of the TNFR1-EGFP cluster (**Fig. 2e**) established a negligible change in the total number of receptor molecules associated with the cluster during 90-second intervals.

Since the intra-cluster reorganization of receptors may alter the rim's IRD, we analyzed whether our method can capture the associated temporal variations of homo-FRET in the rim. Comparison of the temporal variation of relative changes in $\bar{r}_{rim}$ in live (**Fig. 2f**) to the clusters in fixed (**Fig. 2g**) cells demonstrated that our experimental arrangement can monitor the changes in the rim's IRD. Intra-cluster reorganization of receptors in the cluster should lead to fluorescence redistribution across the cluster's core and the rim. **Fig. 2h and 2i** illustrated the normalized time series of the fluorescence fraction in the core ($F_{core}(t)$) in live and fixed cells, respectively. Higher fluctuations of $F_{core}(t)$ in live (**Fig. 2h**) than in fixed (**Fig. 2i**) cells reconfirmed intra-cluster reorganization of the TNFR1-EGFP.

The signaling state of the TNFR1 cluster is linked to the IRD

Fig. 2 revealed that TNFR1-EGFP undergoes continuous and spontaneous intra-cluster reorganization. We, therefore, hypothesized that the ligand sTNF-α enforces intra-cluster rearrangement, provided the cluster contains ligand-free TNFR1-EGFPs. To explore this, we examined changes in the cluster's anisotropy map in response to the activating ligand (sTNF-α) or the inhibitor (zafirlukast). The sTNF-α caused a notable decrease in $\bar{r}_{core}$ and a concomitant increase in $\bar{r}_{rim}$ within the same cluster (**Fig. 3a, 3b**), while maintaining the same cluster area (**Fig. S2a**). This implies intra-cluster rearrangement of TNFR1 molecules, leading to an increase in core's IRD and a decrease in rim's IRD. If the receptor

molecules in the clusters remain unchanged upon sTNF-α introduction, our observations (**Fig. 3a, 3b**) align with three hypotheses: (i) TNFR1 clusters encompass both ligand-bound and ligand-free receptors, (ii) reorganization of TNFR1 molecules within the cluster occurs within the experimental time frame, and (iii) receptors associated with sTNF-α has higher affinity for the core than the rim. Consequently, due to the higher tendency of ligand-bound TNFR1s to reside in the core, rim's IRD decreased upon sTNF-α addition.

In contrast to sTNF-α, zafirlukast treatment resulted in an overall reduction in IRD in both the core and the rim (**Fig. 3c, 3d**), as denoted by the higher r values, while preserving cluster integrity (**Fig. S2a**). The relative changes in the cluster's mean anisotropy (Δr) after 50-60% photobleaching indicated the relative levels of homo-FRET under pre-bleach conditions (*34*, *36*). sTNF-α treatment caused an expected increase in homo-FRET levels within the core (**Fig. 3e**). While we predicted a decrease in homo-FRET levels in the corresponding rim compared to the control, we observed a non-significant change. Furthermore, application of zafirlukast led to a significant reduction in homo-FRET levels in both the core and the rim.

The negative correlation between initial mean anisotropy ($\bar{r}_i$) and the homo-FRET levels as measured by relative changes in corresponding mean anisotropy (Δr) following photobleaching in **Fig. 3f** confirmed significant inter-cluster variations of IRDs in the core. sTNF-α and zafirlukast treatments maintained the correlation between homo-FRET levels and $\bar{r}_i$ (**Fig. 3f**). Similarly, examination of the rim (**Fig. 3g**) reaffirmed lower homo-FRET levels than the core, with sTNF-α minimally affecting rim's IRD. However, zafirlukast reduced IRD in both core and rim, highlighting a preference for sTNF-α-associated receptors to predominantly localize in the core than in the rim.

Next, we explored the relationship between TNFR1 cluster's IRD and signal transduction efficacy. In our study, the nuclear translocation of NF-κB served as an indicator of TNFR1 signal activation. Exposure to sTNF-α activates TNFR1, increasing the nuclear fraction of NF-κB. Thus, the increase in the nuclear-to-cytoplasmic (N/C) ratio of endogenous NF-κB due to sTNF-α indicated the quantitative levels of activation of TNFR1 signaling (**Fig. 3h, S2b**). An increasing dose of sTNF-a caused a higher level of TNFR1 activation leading to gradually increasing levels of NF-κB translocation (**Fig. S2c**). The effect of sTNF-α significantly diminished in TNFR1-depleted HeLa cells, confirming that translocation is mediated through TNFR1 signaling. Zafirlukast reduced the efficacy of sTNF-α (**Fig. 3h, S2d**), and decreased IRD (**Fig. 3d**). We define signaling efficacy as the increase in N/C ratio of NF-κB normalized

by the surface TNFR1 levels for a given dose of sTNF-α. Using both FACS and Western blot analyses, we determined that treatment with zafirlukast or sTNF-α yields no significant change in the level of TNFR1 present on the cell surface (**Fig. 3i**) or in total cellular TNFR1 levels (**Fig. S2e**). We observed an insignificant alteration in the N/C ratio of NF-κB in zafirlukast-treated cells following exposure to sTNF-α (**Fig. 3h**). Thus, the reduced TNFR1 activation by sTNF-α in **Fig. 3h** in the presence of zafirlukast resulted from changes in signaling efficacy rather than alterations in receptor numbers on the cell surface. Furthermore, we noted a correlation between changes in core's IRD (**Fig. 3b, 3d**) and the subsequent responses to sTNF-α (**Fig. 3h**). An increase in the core's IRD correlates with signal activation, while a decrease in IRD impedes the sTNF-α-mediated activation of the TNFR1 cluster.

Additionally, we anticipated that inhibition of PLAD-PLAD interaction by zafirlukast would lead to a loss of TNFR1 receptors from the cluster. Surprisingly, we observed no reduction in the average cluster area estimated through epifluorescence (**Fig. S2a**). However, utilizing TIRF (Total Internal Reflection Fluorescence), we detected a slight yet statistically significant decrease in TNFR-EGFP cluster area following zafirlukast treatment (**Fig. 3j**), suggesting the loss of a small number of receptors from the cluster. Using STED (Stimulated Emission Depletion microscopy), we investigated the fluorescence density of endogenous TNFR1 clusters (**Fig. 3k**), reaffirming the reduction of IRD in zafirlukast-treated condition. Nevertheless, we did not observe a complete disassembly of receptors from the cluster (**Fig. 3i**), suggesting that other interactions besides PLAD-PLAD are responsible for maintaining the integrity of the secondary cluster.

Membrane tension affects the TNFR1 signaling by modulating IRD

After establishing the connection between the IRD and the signaling state of the TNFR1 clusters (**Fig. 3**), we explored the signaling state of the cluster held at varying receptor densities. Cells undergo changes in membrane tension, which can affect the membrane's local curvature (*39–41*) and lipid packing density (*42*), subsequently impacting the TNFR1 cluster's IRD. Consequently, we aimed to study the IRD map of TNFR1-EGFP clusters in cells subjected to elevated or lowered membrane tension. The fluorescence lifetime of Flipper-TR (*43*) revealed that the HeLa cells experience higher membrane tension within 2 minutes after exposure to a hypotonic solution (75% water; **Fig. 4a, S3a**). On the other hand, HeLa cells' membrane tension decreased after exposure to a hypertonic solution for

10 minutes (150 mM mannitol; **Fig. 4b, S3b**). An increase in membrane tension due to hypotonic stress results in a rise in the fluorescence anisotropy within the core and the rim (**Fig. 4c**), suggesting that the IRD within the core and the rim decreases due to increased membrane tension. Conversely, a decrease in membrane tension due to hypertonic stress causes a loss in fluorescence anisotropy in both the core and the rim (**Fig. 4d**), implying an increase in the TNFR1 IRD within the cluster's core and rim.

We utilized membrane tension-driven alterations in IRD (**Fig. 4c, 4d**) to examine the connection between the receptor's density and its signaling efficacy (**Fig. S3c**). Interestingly, the reduction in IRD in hypotonic condition is comparable to that in zafirlukast-treated condition (**Fig. S3d**). While lowering IRD (**Fig. 4c**) in cells did not trigger nuclear translocation of NF-κB (**Fig. 4e**), an increase in IRD (**Fig. 4d**) led to the translocation of NF-κB (**Fig. 4e**). A similar study in cells depleted of TNFR1 (**Fig. 4e**) prevented translocation of NF-κB, establishing NF-κB activation during hypertonic stress was TNFR1-mediated. Since we did not supply additional sTNF-α, we hypothesized that TNFR1 activation in **Fig. 4e** was sTNF-α-independent.

Next, we investigated the signaling efficacy of TNFR1 clusters in cells under hypotonic or hypertonic stress. While we observed reduction of cell surface TNFR1 levels in hypotonic condition, hypertonic stress caused negligible change (**Fig. 4f**). However, the total cellular TNFR1 levels remained same in different osmotic conditions (**Fig. S2e**). Subsequently, we compared the kinetics of NF-κB activation in cells exposed to different osmotic conditions in response to sTNF-α (**Fig. 4g**). Notably, sTNF-α failed to trigger TNFR1-mediated nuclear translocation of NF-κB in cells experiencing hypotonic stress (**Fig. 4g-i**). Despite ligand-free activation of TNFR1 in the hypertonic solution, sTNF-α further triggered nuclear translocation of additional NF-κB (**Fig. 4g-ii**). While the signaling efficacy of TNFR1 under hypotonic conditions reduced significantly, it diminished slightly compared to control under hypertonic conditions (**Fig. 4h**).

We did not detect any significant alteration in the average cluster area under hypotonic and hypertonic stress compared to isotonic conditions, as assessed through epifluorescence imaging (**Fig. S2a**). However, evaluation of cluster area using TIRF indicated a slight decrease in TNFR1-EGFP cluster area under hypo-osmotic conditions relative to isotonic conditions (**Fig. 4i, S3e**) suggesting a loss of a small number of receptors from the cluster. Using STED, we investigated the fluorescence density of endogenous TNFR1 clusters (**Fig. 4j**), reaffirming the reduction of IRD in hypotonic conditions. The decrease in surface receptor levels (**Fig. 4f**) and reduction in average cluster area under hypo-osmotic

stress suggested that increased membrane tension might have led to the dissociation of TNFR1 receptors from the clusters.

3D gel-like micro-environment induces ligand-independent TNFR1 signaling in cells

In our previous work, it was reported that transitioning THP-1 monocytes from a fluid-like (2D) to a gel-like (3D) extracellular microenvironment triggered the nuclear translocation of NF-κB, facilitating inducer-free differentiation into THP-1 macrophages (*44*). However, the specific upstream factors responsible for NF-κB translocation remained uncertain. Like in THP-1 cells, a gel-like extracellular microenvironment induced sTNF-α-independent nuclear translocation of NF-κB in HeLa cells (**Fig. 5a, 5b**). 3D gel-like micro-environment did not alter the cell surface levels of TNFR1 (**Fig. S4a**). Inhibition (**Fig. 5b**) or depletion (**Fig. S4b, S4c**) of TNFR1 prevented the nuclear translocation of NF-κB in a 3D gel-like extracellular microenvironment, confirming the role of TNFR1 in microenvironment-mediated NF-κB activation.

Furthermore, the IRD in both the core and rim increased in the 3D gel-like microenvironment, which was prevented upon administering zafirlukast (**Fig. 5c**). While sTNF-α elevated IRD in the core and diminished it in the rim (**Fig. 3b**), the changes in membrane tension impacted IRD in both the core and the rim in the same direction (**Fig. 5d**). Specifically, increased tension resulted in reduced IRD in both regions, while decreased tension led to increased IRD in both regions (**Fig. 5d**). Thus, a change in IRD across the core and the rim in the same direction indicated a shift in membrane tension in cells. As observed in hypertonic conditions, we predicted that 3D gel-like microenvironment reduces the membrane tension (**Fig. 5d**).

Fig. 5e demonstrated that transitioning cells from a 2D to a 3D microenvironment gradually increased IRD in the cluster's core and rim, signifying a gradual decrease in membrane tension. The lifetime of Flipper-TR confirmed that the 3D gel-like microenvironment reduced membrane tension in HeLa (**Fig. 5f**) and THP-1 cells (**Fig. S4d**). Shifting the cells back to 2D from 3D microenvironment reversed the IRD in the core and the rim (**Fig. 5g**) within 15 minutes. Although the gel-like microenvironment resulted in larger TNFR1-EGFP cluster area (**Fig. 5h**), this increase in area did not bring any correlation between the cluster’s area and the IRD (**Fig. 5i, S4e**).

Disassembly of F-actin or cholesterol depletion decreases IRD to reduce TNFR1 signaling efficacy

The actin cytoskeleton plays a critical role in maintaining cellular structure, organization, and signal transduction. Hence, we investigated how disrupting actin filaments affected sTNF-α-mediated TNFR1 signaling. Cytochalasin D (CytoD)-induced disruption of actin filaments reduced cell surface TNFR1 levels, while disruption of microtubule had negligible impact on the same (**Fig. 6a**). Notably, the total TNFR1 levels remained unchanged with disruption of any of the cytoskeletal filaments (**Fig. S2e**). Additionally, actin filament disruption decreased TNFR1 cluster's IRD in core and rim, while maintaining the average cluster's size (**Fig. 6b, S2a**). Interestingly, microtubule disruption by nocodazole also affected the IRD both in core and rim (**Fig. S5a**).

We then investigated sTNF-α-mediated TNFR1 signaling in CytoD-treated HeLa cells. CytoD induced TNFR1-independent NF-κB translocation via ROS (*45*), confirmed by CytoD-mediated nuclear translocation of NF-κB in TNFR1-depleted cells (**Fig. 6c, S5b**). Vitamin C, a ROS quencher (**Fig. S5c**) (*46, 47*) did not impact the cluster's IRD (**Fig. S5d**), however, it abrogated NF-κB translocation in CytoD-treated cells (**Fig. S5e**). Interestingly, Vitamin C had no discernible effect on sTNF-α-mediated NF-κB translocation in control cells (**Fig. S5e**). **Fig. 6d** compared NF-κB translocation kinetics in control and CytoD-treated cells in response to sTNF-α. Due to decreased IRD in CytoD-treated conditions, we anticipated a significantly retarded rate of NF-κB nuclear translocation compared to control cells. **Fig. 6e** demonstrated that CytoD-induced reduction of TNFR1 IRD diminishes the cluster's signaling efficacy in response to sTNF-α. Additionally, the decrease in IRD (**Fig. S5a**) implied that microtubule disruption could inhibit sTNF-α-mediated activation, consistent with previous observations (*48*).

Cholesterol is an important component of the membrane and is known to affect signaling of various membrane receptors including TNFR1 (*49*). However, the biophysical mechanism remains poorly explored. We anticipated that changes in membrane cholesterol levels might influence the IRD, thereby affecting the signaling efficacy of the TNFR1 cluster. **Fig. 6f** established that reduction in membrane cholesterol levels by MβCD decreased TNFR1 IRD, due to elevated membrane tension (**Fig. 6g**) (*50*). Additionally, evaluation of TNFR1-EGFP cluster area using TIRF indicated a negligible change in cluster area in cholesterol-depleted condition (**Fig. S5f**), suggesting negligible loss of receptors from the cluster. Our investigation established that cholesterol depletion affected IRD, thereby rendering the clusters unresponsive to sTNF-α.

Discussion

The spatial aggregation of transmembrane receptors, including receptor tyrosine kinases (RTK) (*51*), T cell receptors (TCR) (*52*), bacterial chemoreceptors (*53*), and TNFRs, has been recognized for its regulatory function in initiating their respective signaling pathways. The clustering of membrane receptors is anticipated to enhance their sensitivity to extracellular ligands (*54*). Efficient signal activation of TNFR superfamily requires secondary assembly of TNF-TNFR complexes into larger higher-order clusters (**Fig. S6**) (*2, 18, 55*). Activation by sTNF-α brings TNFR1 cytoplasmic domains closer together within the clusters' core, suggesting that elevated density of TNFR1 cytoplasmic domains might be a key factor in modulating signaling (*21*). To date, prevailing research consistently affirms the essential role of TNF-α binding in triggering TNFR1 signaling. However, our study demonstrates that the inherent density within the pre-formed TNFR1 clusters is a parameter that influences signaling. Even in the absence of ligand any alteration in IRD affects the signaling state of the cluster.

To monitor the heterogeneity in IRD across different TNFR1 clusters, we quantified fluorescence anisotropy (r) to assess the energy transfer between TNFR1-EGFP clusters. With a Förster distance of 4.65 nm, EGFP displays a homo-FRET efficiency alteration ranging from 95% to 11% within intermolecular distances of 2.5 to 6.5 nm, rendering it ideal for homo-FRET studies (*56*). Utilizing homo-FRET offers distinct advantages over hetero-FRET when studying homo-oligomeric protein clusters. This method employs only one type of tagged fluorophore bound to the protein of interest, thereby eliminating potential stoichiometric imbalances that may arise during overexpression (*57*).

Alterations in IRD directly influence homo-FRET efficiency, subsequently impacting steady-state fluorescence anisotropy. A higher homo-FRET efficiency leads to a larger loss of polarization and lower r (*58*). Therefore, the cluster's r offers a practical method for live-cell IRD assessment. Moreover, the negative correlation observed between r_i of clusters and the percentage increase in r due to photobleaching (**Fig. 3f, 3g**) (*36, 38*) supports the inverse relationship between the cluster's r map and IRD. Variations in TNFR1 expression levels minimally affect IRD, as depicted in **Fig. 1i**. This suggests that our investigation of IRD remains unaffected by artifacts related to TNFR1 over-expression.

The arbitrary classification of the cluster into core and rim provides insights into intra-cluster receptor dynamics and the effect of IRD on the cluster's signaling state. The receptors inside the cluster constantly undergo spontaneous rearrangement, indicating the dynamic behavior of TNFR1-EGFP molecules within the cluster. As a result, we speculate that the cluster exist as the fluid phase. The dynamic nature of the receptors within the cluster enables ligand-mediated intra-cluster rearrangement of the receptor, which helps alter the IRD. Spontaneous intra-cluster reorganization of TNFR1 (**Fig. 2, 7a**) and rearrangements induced by sTNF-α (**Fig. 3a, 3b, 7b, 7c**) suggest the presence of ligand-free receptors and vacant sites for ligands within the cluster. Literature suggests that the coexistence of ligand-free receptors alongside the cluster enhances the dynamic range of signaling (*54*). Our study elucidates the mechanism through which the dynamic range of signaling expands due to the presence of ligand-free receptors within the cluster. TNFR1's intra-cluster rearrangement due to vacant sites enables localized modulation of the core's IRD, facilitating signal modulation with sTNF-α. Zafirlukast treatment reduces IRD in the cluster's core and rim as expected (**Fig. 7b, 7d**), reaffirming that the TNFR1-EGFP cluster's anisotropy image reflects the IRD map.

Experimentally manipulating the TNFR1 IRD while preserving other biochemical elements of the cellular system poses a considerable challenge. The physical microenvironment surrounding cells plays a crucial role in their behavior and activity, primarily by affecting membrane dynamics. By modifying the extracellular microenvironment using a non-interacting agarose medium, we aimed to specifically investigate the isolated effect of the environment without any other interference. Intriguingly, subjecting HeLa cells to hypertonic, hypotonic, or 3D gel-like microenvironments (**Fig. 7b, 7e**), which alter membrane tension, results in changes in IRD. Under these conditions, an increase in IRD leads to self-activation of TNFR1 signaling, while a decrease in IRD renders the TNFR1 clusters insensitive to sTNF-α (**Fig. 7b, 7d**), indicating that IRD serves as a switch controlling the cluster's signaling state (*59*). **Fig. 3 and 4** determine that a reduction in membrane tension under hypertonic conditions and within a 3D gel-like microenvironment induces IRD-mediated TNFR1 signal activation, even in the absence of additional ligand stimulation. The substantial intra-cluster variations in r_{core} and r_{rim} suggest the existence of different clusters in distinct signaling states. Furthermore, a significant portion of the plasma membrane remains near the dense F-actin network of the actin cortex. **Fig. 6** illustrates that the actin cytoskeleton along with the cholesterol, maintains TNFR1 clusters in a ligand-sensitive state, and

any disruption of actin cytoskeletal structure or depletion of cholesterol (**Fig. 7b, 7d**) hinders the TNFR1 signaling process.

In conclusion, our findings strongly support the direct influence of TNFR1 IRD on the signaling state of the cluster. The utilization of homo-FRET for investigating IRD presents an opportunity to explore the clustering of other receptors and subsequent activation of downstream signaling pathways. Alterations in TNFR1 clustering can result in dysfunctional signal transduction, which is detrimental to cellular health. Therefore, our study aims to explore both the ligand-dependent and ligand-independent modes of TNFR1 signaling induced by changes in receptor density at the membrane level. We deduce that alterations in the IRD are adequate to either initiate or impede signaling, regardless of the presence of any ligand.

Materials and Methods

Plasmids

The following plasmids were obtained from Addgene: pTNFR1-tdEOS, a contribution from Mike Heilemann (#98273); mEGFP-N1, provided by Michael Davidson (#54767); and EGFP-p65, gifted by Johannes A. Schmidd (#111190). The 2GFP (GFP-GFP) plasmid was generously provided by Prof. Maria Vartiainen from the University of Helsinki, Finland. The TNFR1-EGFP plasmid was constructed by sub-cloning the TNFR1 gene from the pTNFR1-tdEOS plasmid into the N-terminal of the mEGFP-N1 plasmid, with a flexible linker of 14 amino acids in between. The full-length human TNFR1 gene sequence was amplified by polymerase chain reaction (PCR) using the following primers:

5’-cggagctc**gccacc**ATGGGCCTCTCCACCGTGCCTG-3’ (forward)

5’-gtgtcgactcTCTGAGAAGACTGGGCGCGGGCGGGAGGGC-3’ (reverse)

The overhangs containing the restriction endonuclease sites (underlined) and the Kozak sequence (bold) are indicated in lowercase. The purified PCR product was inserted into the multiple cloning site (MCS) of the mEGFP-N1 vector backbone to generate C-terminally tagged TNFR1-EGFP. SacI (QuickCutTM Sac I, Takara Bio, #1627) and SalI (QuickCutTM Sal I, Takara Bio, #1636) restriction endonucleases were used. The digested products were ligated using T4 DNA Ligase (New England Biolabs, #M0202S). The fidelity of the chimeric clone was confirmed through diagnostic restriction digestion and direct sequencing (Eurofins, Bangalore, India).

Cell culture and transfection

HeLa cell line was obtained from the National Center for Cell Science (NCCS) in Pune, India, while THP-1 cell line of American Type Culture Collection (ATCC) origin was generously provided by Dr. Prosenjit Sen from the Indian Association for the Cultivation of Science in Kolkata, India. Both cell lines were cultured in Dulbecco’s Modified Eagle Medium (DMEM) (HiMedia, #AL007G) supplemented with 10% fetal bovine serum (FBS) (HiMedia, #RM9955) and 1% penicillin-streptomycin (Antibiotic Solution 100X Liquid, HiMedia, #A001) at 37°C in a humidified incubator with 5% CO2.

HeLa cells were transfected with the afore-mentioned plasmids using FuGENE® HD Transfection Reagent (Promega, #E2311), following the manufacturer's protocol. Approximately 1 x 10^5 cells were seeded in glass-bottom Petri dishes 24 hours before transfection and allowed to reach 70% confluency. Transfection was carried out using 1 μg of plasmid DNA under serum-starved conditions, and the cells were incubated overnight at 37°C with 5% CO2. The medium was then replaced with DMEM supplemented with FBS and antibiotics before proceeding with further experiments. To generate TNFR1 knockdown cells, HeLa cells were transfected with pre-designed siRNA targeting human TNFRSF1A (Sigma-Aldrich/Merck, #SASI_Hs01_00033456, #SASI_Hs01_00033458), along with MISSION® siRNA Universal Negative Control #1 (Sigma-Aldrich/Merck, #SIC001) as the corresponding scrambled control. The transfection was performed using 30nM siRNA and FuGENE® under serum-starved conditions following the standard protocol. The transfection mix was incubated at room temperature for 15 minutes before being added drop-wise to the cells. The silenced cells were analyzed 96 hours post-transfection. To validate TNFR1-mediated NF-κB nuclear translocation in 3D gel-like microenvironment, cells were pre-treated with 50 μM zafirlukast (Sigma-Aldrich/Merck, #Z4152) for 16 hours before proceeding with EGFP-p65 transfection.

sTNF-α, drug, and osmolyte treatments

To initiate cytokine stimulation, HeLa cells (1 x 10^5) were plated in glass-bottomed Petri dishes and incubated overnight at 37°C with 5% CO2. Subsequently, to deplete secreted cytokines and minimize cellular metabolic activity, the existing DMEM was aspirated, and cells were subjected to serum starvation for 4 hours. Afterward, cells were thoroughly rinsed twice with serum-free DMEM to eliminate any soluble tumor necrosis factor-alpha (sTNF-α) that might be present in the medium. Recombinant human TNF-α protein (ABclonal, #RP00993) was then introduced to the cells at various concentrations (5-100 ng/mL) and for different durations (5-30 minutes), as specified in the results section.

To administer zafirlukast (Sigma-Aldrich/Merck, #Z4152), cells underwent a serum starvation period of 3 hours, followed by incubation with 100 μM zafirlukast for 1 hour. To induce osmotic shock in HeLa cells, the standard isotonic DMEM was replaced with hypertonic media (150 mM mannitol (Sigma-Aldrich/Merck, #M9647) dissolved in DMEM) or hypotonic media (75% autoclaved distilled water mixed with 25% DMEM by volume) for the duration specified in the results section. Additionally,

to disrupt the actin cytoskeleton, HeLa cells were treated with 2 μM cytochalasin D (CytoD) (Sigma-Aldrich/Merck, #C8273) under serum-starved conditions for 1 hour, unless otherwise stated. Cholesterol depletion in HeLa cells involved a serum starvation for 2 hours, followed by 1 hour incubation with 2 mM methyl-β-cyclodextrin (MβCD) (Sigma-Aldrich/Merck, #C4555).

Immunofluorescence

HeLa cells were seeded in a glass-bottom plate and incubated overnight in cell culture conditions. They were then fixed with 4% paraformaldehyde (PFA) (HiMedia, #GRM3660) in 1x phosphate-buffered saline (PBS) for 15 minutes. For immunostaining of the plasma membrane-associated TNFR1, the fixed cells were blocked with a 5% BSA solution in 1x PBS for 1 hour at room temperature, without permeabilizing the plasma membrane. After three washes with 1x PBS, the cells were incubated with a 1:500 dilution of TNFR1/TNFRSF1A rabbit pAb (ABclonal, #A1540) in antibody dilution buffer (3% BSA in 1x PBS) overnight at 4°C. Subsequently, the cells were washed thrice with 1x PBS and incubated with Alexa Fluor-594 conjugated secondary antibody (1:200 dilution, Anti-rabbit IgG, Cell Signaling Technology, #8889) for 1 hour at room temperature. After three washes with 1x PBS, the cells were ready for imaging. To validate our TNFR1-EGFP chimeric construct, HeLa cells were transfected with TNFR1-EGFP and incubated for 18-20 hours. After this incubation period, the cells were fixed and prepared for membrane-associated TNFR1 immunostaining following the protocol described above. This approach allowed us to visualize most plasma-membrane-associated TNFR1-EGFP expressions (**Fig. S1b**) of the TNFR1-EGFP chimeric construct within the cells.

For immunostaining of NF-κB (p65) after fixation of the HeLa cells with 4% PFA in 1x PBS for 15 mins, they were permeabilized with 0.1% Triton X-100 (Sisco Research Laboratories, #64518) in 1x PBS for 4-5 mins. Then the fixed cells were blocked with a 5% BSA solution in 1x PBS for 1 hour at room temperature. After three washes with 1x PBS, the cells were incubated with a 1:500 dilution of NF-κB p65 mouse mAb (Cell Signaling Technology, #6956) in antibody dilution buffer (3% BSA in 1x PBS) overnight at 4°C. Subsequently, the cells were washed thrice with 1x PBS and incubated with Alexa Fluor-594 conjugated secondary antibody (1:200 dilution, Anti-mouse IgG, Cell Signaling Technology, #8890) for 1 hour at room temperature. After three washes with 1x PBS, the cells were ready for imaging. The nuclei were counterstained with Hoechst 33342 (ThermoFisher, #62249) (0.5 μg/mL, 5 minutes).

Cell extracts and immunoblotting

HeLa cells (1 x 10^5) were cultured in 35 mm dishes and incubated overnight at 37°C with 5% CO2 until reaching approximately 70% confluency. Following this, the cells were either transfected with siRNA or treated with various drugs for specified durations before proceeding with cell lysate preparation. The cells were rinsed with ice-cold PBS and then lysed using 100 µL of RIPA buffer (50 mM Tris HCl, 150 mM NaCl, 1.0% (v/v) NP-40, 0.5% (w/v) sodium deoxycholate, 1.0 mM EDTA, 0.1% (w/v) SDS, and 0.01% (w/v) sodium azide, pH 7.4), supplemented with Protease and Phosphatase Inhibitor Cocktail (Sigma-Aldrich/Merck, #PPC1010). The lysates were incubated on ice for 15 minutes, and then the contents of each dish were transferred to respective 1.5 mL microcentrifuge tubes. Total cell extracts were obtained by agitating the lysates at 4°C for 30 minutes. The cell lysates were centrifuged at 12,000 g for 20 minutes at 4°C, and the supernatants were collected in fresh tubes kept on ice.

The protein concentration was determined using the Bradford assay, and subsequently, 40-50 µg of total protein per condition was loaded onto a 12% polyacrylamide gel after boiling the samples in 2X Laemmli sample buffer (4% (w/v) SDS, 20% (v/v) glycerol, 120 mM Tris-HCl pH 6.8, 0.02% bromophenol blue) containing 5% β-mercaptoethanol for 15 minutes. The samples were then immediately resolved on SDS-polyacrylamide gel electrophoresis (PAGE), and the proteins were transferred to Immobilon®-P PVDF membrane (Merck Millipore, #IPVH00010). Immunoblots were blocked with 5% bovine serum albumin (BSA) in tris-buffered saline (TBS) containing 0.1% Tween-20 (TBS-T) for 1 hour at room temperature. The membrane was then probed with specific primary antibodies diluted 1:1000 in antibody dilution buffer (3% BSA in TBS-T) and incubated overnight at 4°C - either anti-TNFR1 rabbit monoclonal antibody (Invitrogen, #MA5-14899) or anti-β-Actin mouse monoclonal antibody (Santa Cruz Biotechnology, #sc-47778). Following primary antibody incubation, the membranes were washed thrice with TBS-T for 5 minutes each and then incubated with the respective secondary antibodies at room temperature for 1 hour - either 1:10,000 horseradish peroxidase (HRP)-conjugated goat anti-rabbit IgG (Sigma-Aldrich/Merck, #A9169) or anti-mouse IgG (Sigma-Aldrich/Merck, #A9044). Protein detection was performed following the enhanced chemiluminescence procedure, and a Pre-stained Protein Ladder (HiMedia, #MBT092) was used to determine the molecular weight of the proteins of interest.

Flow cytometry

HeLa cells (1 x 10^5) were cultured in 35 mm Petri dishes overnight for 16 hours under standard cell culture conditions. Following this, the cells were exposed to various treatments as described in the results section. After each treatment, the cells were fixed with 4% paraformaldehyde (PFA) at room temperature for 15 minutes. Subsequently, the cells were washed three times with ice-cold 1x phosphate-buffered saline (PBS) and then proceeded with immunostaining of plasma membrane-associated TNFR1 as previously described. After incubation with the Alexa Fluor-488 conjugated secondary antibody (1:200 dilution, Anti-rabbit IgG, Cell Signaling Technology, #4412), the cells underwent three washes with ice-cold 1x PBS. Subsequently, the cells were gently scraped and suspended in 1x PBS to prepare them for flow cytometric analysis. A total of 10^4 cells were recorded for each condition in the FITC channel to measure the cell surface expression of TNFR1 relative to unstained and control conditions. Data acquisition was performed using a BD FACS Aria III, and the respective normalized mean fluorescence intensities (MFI) were plotted using Origin 2019b. The signaling efficacy of TNFR1 was quantified by determining the mean p65 N/C ratio per plasma membrane-associated TNFR1 molecule, calculated using the MFI obtained from flow cytometry in each condition (with or without sTNF-α).

TNFR1-EGFP chimeric construct validation and cluster area analysis using confocal microscopy

To validate the TNFR1-EGFP chimeric construct, TNFR1 was immunostained in TNFR1-EGFP overexpressing cells without plasma membrane permeabilization. The cells were imaged using a Zeiss LSM 780 light scanning confocal system with a 63x oil immersion objective, using two channels for green (TNFR1-EGFP) and red (Alexa Fluor-594, endogenous) fluorescence. Merging the two channels resulted in yellow color in the TNFR1-EGFP cluster regions, indicating colocalization, and confirming that the anti-TNFR1 pAb recognizes our TNFR1-EGFP construct.

For TNFR1 cluster area measurements images were captured using a Zeiss LSM 780 light scanning confocal system with a 63x oil immersion objective in airy scan mode. Then the TNFR1 clusters, both endogenous and overexpressed (TNFR1-EGFP), were segregated using intensity-based thresholding in ImageJ, and the area of the clusters was measured using the segregated ROI in measurement plugins.

Quantification of TNFR1-EGFP clusters on the plasma membrane over time

HeLa cells overexpressing TNFR1-EGFP were stained with 0.5x CellMask Orange (CellMask™ Plasma Membrane Stains, Invitrogen, #C10045) at 4-, 12-, 18-, and 24-hours post-transfection. The live HeLa cells overexpressing TNFR1-EGFP and stained with CellMask Orange were imaged using a Zeiss LSM 780 light scanning confocal system. The imaging was performed with a 63x oil immersion objective in airy scan super-resolution mode, with a 0.4μm Z-step size, using two appropriate channels for green (EGFP) and orange (CellMask Orange) fluorescence. Image analysis was performed in ImageJ, where the cell boundary was determined from the CellMask Orange image using intensity-based thresholding. Clusters of TNFR1-EGFP that overlapped with the CellMask Orange-derived cell boundary were classified as plasma membrane-associated clusters. Total and plasma membrane-associated TNFR1-EGFP cluster counting of a cell was conducted using the 3D object counter plugin in ImageJ. The percentage of fractional plasma membrane-associated clusters was then calculated at different time points.

Nuclear-to-cytoplasmic (N/C) p65 measurement

Fluorescence images of p65-immunostained HeLa cells were captured using a Zeiss AxioObserver Z1 microscope with a 40x air objective to measure the nuclear-to-cytoplasmic ratio (N/C). Z-stacks of randomly selected cell populations were obtained for analysis. Image analysis using ImageJ was performed to determine the N/C ratio of p65. The nuclear portion of p65 was quantified by selecting a region of interest (ROI) in the focused Z-plane of the nucleus, as identified from Hoechst staining images. The mean fluorescence intensity of nuclear p65 (N) was measured using this ROI from the p65 immunostaining z-stack image. For cytoplasmic p65 (C), the total fluorescence intensity of the cytoplasm was measured in areas where the cytoplasm was in focus. The total nuclear fluorescence intensity was then subtracted from this value. The mean cytoplasmic p65 intensity was calculated by dividing the total cytoplasmic intensity by the cytoplasmic area, which was determined by subtracting the nuclear area from the total protoplasmic area.

Cell culture in a 3D gel-like microenvironment

HeLa cells (1×10^5) were seeded in a glass-bottom Petri dish and allowed to adhere overnight under standard cell culture conditions. Subsequently, the medium was aspirated, and a solution of 1% low-melting HiRes Agarose (Genetix, Puregene, #PG-432) in DMEM was carefully added to cover the

adherent cells, forming a thin gel layer. The Petri dish was then briefly incubated at 4°C for 2 minutes to facilitate rapid gel formation. Fresh media was gently added on top of the agarose gel cover to prevent dehydration. The cells were maintained within this 3D gel-like microenvironment for the durations specified in the results section.

ROS measurements

HeLa cells were seeded in a 96-well plate at equal density (1 x 10^4 cells) and allowed to grow for 24 hours. Subsequently, the cells were treated with 2 μM cytochalasin D (CytoD) (Sigma-Aldrich/Merck, #C8273) for 1 hour, with or without pre-treatment with 500 μM L-Ascorbic acid (Vitamin C) (Sigma-Aldrich/Merck, #A4544) for 1 hour. For reactive oxygen species (ROS) analysis, cells were stained with 10 μM H2DCFDA (Sigma-Aldrich/Merck, #287810) for 30 minutes following each treatment and then lysed with 95% dimethyl sulphoxide (DMSO) (HiMedia, #MB058). The fluorescence intensity of each cell sample was measured using a spectrofluorometer (SpectraMax iD5 Multi-Mode Microplate Reader, Molecular Devices) with excitation/emission wavelengths set at 485 nm/535 nm.

Fluorescence Anisotropy Imaging Microscopy (FAIM)

Fluorescence anisotropy of TNFR1-EGFP was measured in HeLa cells overexpressing the protein, 18-20 hours post-transfection. The fluorescence anisotropy was determined using a well-established principle (*35*). Imaging was performed with a Zeiss AxioObserver Z1 epifluorescence microscope equipped with a 63x oil immersion objective (NA 1.4) and a mercury arc lamp (HXP 120 V) as the light source. Horizontally polarized excitation light was achieved by passing the light through a linear polarizer (ThorLabs) in the excitation path. In the emission path, a polarizing beam splitter (DV2, Photometrics) was utilized to divide the resulting polarized fluorescence signal into parallel and perpendicular polarizations. The fluorescence from these two polarizations was simultaneously captured by a CMOS camera (Hamamatsu Orca Flash 4.0 C13440), with one half of the image representing the parallel channel ($I_{\parallel}$) and the other half representing the perpendicular channel ($I_{\perp}$). Due to deformations in the optical path and thermal fluctuations, there was partial overlap between the two halves ($I_{\parallel}$, $I_{\perp}$). To correct this, image registration of each cluster of TNFR1-EGFP in the two channels was performed by intensity cross-correlation using the particle image velocimetry (PIV) method

followed by MATLAB's mono-modal intensity-based registration tool (**Fig. S1h**). Subsequently, the fluorescence anisotropy (r) in each pixel of the clusters was calculated using the equation:

$$r = \frac{I_{\parallel} - g\, I_{\perp}}{I_{\parallel} + 2\, g\, I_{\perp}}$$

Where g is the instrumental correction factor (G-factor, $I_{\parallel}/I_{\perp}$), determined by measuring 100 nM fluorescein in water in each pixel. A custom MATLAB code was developed for TNFR1-EGFP cluster image registration and anisotropy calculation. Verification of homo-FRET was carried out through sequential photobleaching at 100% lamp power for 20 seconds, with imaging of the same cell before and after photobleaching. Background correction was performed by subtracting the mean fluorescence intensity of regions without transfected cells in the imaging field. The fluorescence anisotropy of HeLa-mEGFP and HeLa-2GFP cells was assessed using in-house ImageJ code. To achieve image registration, fluorescent polystyrene microspheres with a 200 nm diameter were dried onto a glass coverslip and imaged in the same configuration as the anisotropy measurements. The Descriptor-based Registration plugin of Fiji (ImageJ) was employed for this purpose.

From the anisotropy calculation of TNFR1-EGFP clusters, we obtained a total intensity map ($I_{\parallel} + 2\, g\, I_{\perp}$) and a fluorescence anisotropy map (r) for each cluster. To simplify our analysis, we divided the fluorescence anisotropy map of each TNFR1-EGFP cluster into two regions, which we named core (central region) and rim (peripheral region), based on the intensity map. In the intensity map, the region with intensity greater than or equal to 70% of the maximum intensity of the cluster was designated as the core, while the region with intensity greater than 10% of the maximum intensity was considered the whole cluster. The rim region was then obtained by subtracting the core region from the whole cluster. Therefore, the rim region comprised the intensity values between >10% to <70% of the maximum intensity of the cluster (**Fig. 1d-iii, 1d-iv, 1e**). A custom ImageJ code was developed to perform this segmentation. Using the same region of interest (ROI) from the intensity map, we extract the core and rim anisotropy values from the anisotropy map.

Fluorescence Lifetime Imaging Microscopy (FLIM)

Flipper-TR (Spirochrome, #SC020) was used to assess the plasma membrane tension of cells through fluorescence lifetime imaging. Fluorescence lifetime measurements of Flipper-TR were conducted

using an Olympus IX71 microscope with a 60x water immersion objective (NA 1.2) fitted with a time-correlated single-photon counting (TCSPC) module from PicoQuant, and excited with a picosecond 470 nm laser (PicoQuant). The fluorescence lifetime data for each pixel were analyzed by fitting them to a bi-exponential decay curve using SymPhoTime64 software. To quantify the lifetime, the higher amplitude lifetime (τ_1) at each pixel was used, as detailed in the referenced article (*42*). For each cell, τ_1 values were averaged over the region of interest (ROI) corresponding to the plasma membrane. HeLa Cells were first incubated with 200 nM Flipper-TR for 15 minutes in isotonic conditions before undergoing hypo- and hypertonic treatments. To assess the effect of 3D gel-like microenvironment on membrane tension, both control (2D) and cells covered with non-interacting low-melting agarose (3D) were incubated with 200 nM Flipper-TR overnight in HeLa cells and for 4 hours in THP-1 cells.

Fluorescence Recovery after Photobleaching (FRAP)

FRAP experiments were conducted on HeLa cells overexpressing TNFR1-EGFP using a Zeiss LSM 780 light scanning confocal system with a 63x oil immersion objective. TNFR1-EGFP clusters were first imaged with 2% laser power and then bleached using 60% laser power at 488 nm, followed by the acquisition of time-lapse imaging for 90 seconds with 1-second intervals using 2% laser power of the same region. The percentage of recovery after bleaching was calculated relative to the pre-bleached condition by comparing the mean fluorescence intensity of the clusters over time to the pre-bleach mean fluorescence intensity. This value was then plotted against time to visualize the recovery process.

IRM

Cell imaging was conducted on a Nikon Eclipse Ti-E motorized inverted microscope (Nikon, Japan), featuring adjustable field and aperture diaphragms, a 60X Plan Apo lens (NA 1.22, water immersion), and a 1.5X external magnification. The microscope was positioned on an onstage 37°C incubator (Tokai Hit, Japan). Imaging was facilitated using an s-CMOS camera (ORCA Flash 4.0, Hamamatsu, Japan). Illumination was provided by a 100W mercury arc lamp, employing an interference filter (546±12 nm) and a 50-50 beam splitter. For Interference Reflection Microscopy (IRM), movies comprised 2048 frames (20 frames/s), recorded with an exposure time of 50 ms. Analysis of IRM images to obtain fluctuation tension was performed (*60*) using three different steps. At first the calibration factor is obtained to convert intensity to relative height and pixels corresponding to the first branch region (FBR)

of the interference pattern are identified. Subsequently the timeseries of height obtained for each pixel and the amplitude of fluctuations (SD_{time} and SD_{space}) obtained for FBRs. Finally, for every FBR the power spectral density (PSD) obtained and fitted to an adapted Helfrich-Calham model to extract the fluctuation tension and other parameters (*61*).

TIRF imaging

TIRF Microscopy utilized an inverted microscope (Olympus IX-83, Olympus, Japan) equipped with a 100X 1.49 NA oil immersion TIRF objective (PlanApo, Olympus). The imaging setup included an s-CMOS camera (ORCA Flash 4.0, Hamamatsu, Japan) and a 488 nm laser source. Image acquisition was performed with an exposure time of 200 ms, achieving a penetration depth of approximately 70 nm. For cluster size analysis from TIRF images, local thresholding was performed to detect objects using MATLAB. All immobile clusters were manually identified and the area of the objects from the region properties were used for comparison.

STED imaging

For STED experiments, cells were initially fixed with 4% PFA for 15 minutes and then subjected to two washes with PBS. Following this, cells underwent a 5-minute incubation in 0.1 M glycine (Sigma-Aldrich, #G8898) and were again washed with PBS. A 2-minute treatment with Triton X-100 was applied, followed by another wash with PBS. For blocking, cells were exposed to an overnight incubation at 4°C with 3 mL of a 0.2% gelatin solution (Sigma-Aldrich, #G2500). Primary antibody treatment involved the use of anti-TNFR1 rabbit antibody (ABclonal, #A1540) at a 1:200 dilution in gelatin for 2 hours at room temperature; followed by goat anti-rabbit IgG STAR RED (Abberior, #STRED-1002-500UG) at a 1:400 dilution in gelatin for 2 hours after a PBS wash.

STED imaging was conducted using an Abberior Facility Line system integrated with an Olympus IX83 microscope from Abberior instruments. The Abberior auto-alignment sample was utilized for aligning the STED and confocal channels. Throughout the imaging process, a consistent 15 nm pixel size was maintained. Depletion during imaging was achieved using a pulsed STED line at 775 nm, and the visualization of TNFR1 utilized STAR RED conjugated goat anti-rabbit secondary antibody. To analyze the size of TNFR1 clusters, STED images were processed by performing local thresholding to detect objects using MATLAB.

Statistical analysis

Individual measurements from technical replicates within a particular treatment group were pooled to create a unified set of biological replicates for each dataset. Variations in mean values of measurements taken from the same cells before and after treatment were evaluated through the paired sample T-test (**Fig. 3b, 4i, S3e**). In instances where measurements were obtained from distinct cell groups, the unpaired T-test was employed to compare population averages, under the assumption that sufficiently large sample sizes would exhibit a normal distribution (**Fig. 1-6**). Statistical analyses and graphical representation of data were conducted using Origin 2019b.

References

1. H. T. Idriss, J. H. Naismith, TNFα and the TNF receptor superfamily: Structure-function relationship(s). *Microsc Res Tech* **50**, 184–195 (2000).
2. É. S. Vanamee, D. L. Faustman, Structural principles of tumor necrosis factor superfamily signaling. *Sci Signal* **11** (2018).
3. M. Croft, W. Duan, H. Choi, S.-Y. Eun, S. Madireddi, A. Mehta, TNF superfamily in inflammatory disease: translating basic insights. *Trends Immunol* **33**, 144–152 (2012).
4. G. van Loo, M. J. M. Bertrand, Death by TNF: a road to inflammation. *Nat Rev Immunol* **23**, 289–303 (2023).
5. Y. Takei, R. Laskey, Tumor Necrosis Factor α Regulates Responses to Nerve Growth Factor, Promoting Neural Cell Survival but Suppressing Differentiation of Neuroblastoma Cells. *Mol Biol Cell* **19**, 855–864 (2008).
6. A. Bhardwaj, B. B. Aggarwal, Receptor-mediated choreography of life and death. *J Clin Immunol* **23**, 317–32 (2003).
7. O. Micheau, J. Tschopp, Induction of TNF Receptor I-Mediated Apoptosis via Two Sequential Signaling Complexes. *Cell* **114**, 181–190 (2003).
8. S. Yang, C. Xie, Y. Chen, J. Wang, X. Chen, Z. Lu, R. R. June, S. G. Zheng, Differential roles of TNFα-TNFR1 and TNFα-TNFR2 in the differentiation and function of CD4+Foxp3+ induced Treg cells in vitro and in vivo periphery in autoimmune diseases. *Cell Death Dis* **10**, 27 (2019).
9. J. D. Webster, D. Vucic, The Balance of TNF Mediated Pathways Regulates Inflammatory Cell Death Signaling in Healthy and Diseased Tissues. *Front Cell Dev Biol* **8** (2020).
10. G. Chen, D. V. Goeddel, TNF-R1 Signaling: A Beautiful Pathway. *Science (1979)* **296**, 1634–1635 (2002).
11. R. A. Smith, C. Baglioni, The active form of tumor necrosis factor is a trimer. *Journal of Biological Chemistry* **262**, 6951–6954 (1987).
12. J. H. Naismith, B. J. Brandhuber, T. Q. Devine, S. R. Sprang, Seeing double: Crystal structures of the type I TNF receptor. *Journal of Molecular Recognition* **9**, 113–117 (1996).

13. D. W. Banner, A. D'Arcy, W. Janes, R. Gentz, H.-J. Schoenfeld, C. Broger, H. Loetscher, W. Lesslauer, Crystal structure of the soluble human 55 kd TNF receptor-human TNFβ complex: Implications for TNF receptor activation. *Cell* **73**, 431–445 (1993).
14. C. Karathanasis, J. Medler, F. Fricke, S. Smith, S. Malkusch, D. Widera, S. Fulda, H. Wajant, S. J. L. van Wijk, I. Dikic, M. Heilemann, Single-molecule imaging reveals the oligomeric state of functional TNFα-induced plasma membrane TNFR1 clusters in cells. *Sci Signal* **13**, 5647 (2020).
15. K. Kucka, H. Wajant, Receptor Oligomerization and Its Relevance for Signaling by Receptors of the Tumor Necrosis Factor Receptor Superfamily. *Front Cell Dev Biol* **8** (2021).
16. F. Fricke, S. Malkusch, G. Wangorsch, J. F. Greiner, B. Kaltschmidt, C. Kaltschmidt, D. Widera, T. Dandekar, M. Heilemann, Quantitative single-molecule localization microscopy combined with rule-based modeling reveals ligand-induced TNF-R1 reorganization toward higher-order oligomers. *Histochem Cell Biol* **142**, 91–101 (2014).
17. F. K.-M. Chan, H. J. Chun, L. Zheng, R. M. Siegel, K. L. Bui, M. J. Lenardo, A Domain in TNF Receptors That Mediates Ligand-Independent Receptor Assembly and Signaling. *Science (1979)* **288**, 2351–2354 (2000).
18. É. S. Vanamee, D. L. Faustman, The benefits of clustering in TNF receptor superfamily signaling. *Front Immunol* **14** (2023).
19. M. Branschädel, A. Aird, A. Zappe, C. Tietz, A. Krippner-Heidenreich, P. Scheurich, Dual function of cysteine rich domain (CRD) 1 of TNF receptor type 1: Conformational stabilization of CRD2 and control of receptor responsiveness. *Cell Signal* **22**, 404–414 (2010).
20. L. Zhao, Q. Fu, L. Pan, A. Piai, J. J. Chou, The Diversity and Similarity of Transmembrane Trimerization of TNF Receptors. *Front Cell Dev Biol* **8** (2020).
21. P. E. Morton, C. Perrin, J. Levitt, D. R. Matthews, R. J. Marsh, R. Pike, D. Mcmillan, A. Maloney, S. Poland, S. Ameer-Beg, M. Parsons, "TNFR1 membrane reorganization promotes distinct modes of TNFα signaling" (2019); http://stke.sciencemag.org/.
22. M. P. Boldin, I. L. Mett, E. E. Varfolomeev, I. Chumakov, Y. Shemer-Avni, J. H. Camonis, D. Wallach, Self-association of the "Death Domains" of the p55 Tumor Necrosis Factor (TNF) Receptor and Fas/APO1 Prompts Signaling for TNF and Fas/APO1 Effects. *Journal of Biological Chemistry* **270**, 387–391 (1995).
23. A. Caminero, M. Comabella, X. Montalban, Tumor necrosis factor alpha (TNF-α), anti-TNF-α and demyelination revisited: An ongoing story. *J Neuroimmunol* **234**, 1–6 (2011).
24. A. Caminero, M. Comabella, X. Montalban, Role of tumour necrosis factor (TNF)-α and *TNFRSF1A* R92Q mutation in the pathogenesis of TNF receptor-associated periodic syndrome and multiple sclerosis. *Clin Exp Immunol* **166**, 338–345 (2011).
25. F. C. Kimberley, A. A. Lobito, R. M. Siegel, G. R. Screaton, Falling into TRAPS – receptor misfolding in the TNF receptor 1-associated periodic fever syndrome. *Arthritis Res Ther* **9**, 217 (2007).
26. G.-M. Deng, L. Zheng, F. K.-M. Chan, M. Lenardo, Amelioration of inflammatory arthritis by targeting the pre-ligand assembly domain of tumor necrosis factor receptors. *Nat Med* **11**, 1066–72 (2005).
27. F. Hadziselimovic, L. R. Emmons, H. Gallati, Soluble tumour necrosis factor receptors p55 and p75 in the urine monitor disease activity and the efficacy of treatment of inflammatory bowel disease. *Gut* **37**, 260–3 (1995).
28. A. A. Lobito, F. C. Kimberley, J. R. Muppidi, H. Komarow, A. J. Jackson, K. M. Hull, D. L. Kastner, G. R. Screaton, R. M. Siegel, Abnormal disulfide-linked oligomerization results in ER retention and altered

signaling by TNFR1 mutants in TNFR1-associated periodic fever syndrome (TRAPS). *Blood* **108**, 1320–1327 (2006).

29. Y.-F. Chen, P. Jobanputra, P. Barton, S. Jowett, S. Bryan, W. Clark, A. Fry-Smith, A. Burls, A systematic review of the effectiveness of adalimumab, etanercept and infliximab for the treatment of rheumatoid arthritis in adults and an economic evaluation of their cost-effectiveness. *Health Technol Assess (Rockv)* **10** (2006).
30. H. Wajant, Principles of antibody-mediated TNF receptor activation. *Cell Death Differ* **22**, 1727–41 (2015).
31. X. Yu, S. James, J. H. Felce, B. Kellermayer, D. A. Johnston, H. T. C. Chan, C. A. Penfold, J. Kim, T. Inzhelevskaya, C. I. Mockridge, Y. Watanabe, M. Crispin, R. R. French, P. J. Duriez, L. R. Douglas, M. J. Glennie, M. S. Cragg, TNF receptor agonists induce distinct receptor clusters to mediate differential agonistic activity. *Commun Biol* **4**, 772 (2021).
32. M. Grell, H. Wajant, G. Zimmermann, P. Scheurich, The type 1 receptor (CD120a) is the high-affinity receptor for soluble tumor necrosis factor. *Proceedings of the National Academy of Sciences* **95**, 570–575 (1998).
33. N. Weinelt, C. Karathanasis, S. Smith, J. Medler, S. Malkusch, S. Fulda, H. Wajant, M. Heilemann, S. J. L. van Wijk, Quantitative single-molecule imaging of TNFR1 reveals zafirlukast as antagonist of TNFR1 clustering and TNFα-induced NF-κB signaling. *J Leukoc Biol* **109**, 363–371 (2021).
34. S. Ghosh, S. Saha, D. Goswami, S. Bilgrami, S. Mayor, “Dynamic Imaging of Homo-FRET in Live Cells by Fluorescence Anisotropy Microscopy” (2012), pp. 291–327.
35. J. R. Lakowicz, Principles of fluorescence spectroscopy. *Principles of Fluorescence Spectroscopy*, 1–954 (2006).
36. S. Ganguly, A. H. A. Clayton, A. Chattopadhyay, Organization of higher-order oligomers of the serotonin$_1$(A) receptor explored utilizing homo-FRET in live cells. *Biophys J* **100**, 361–8 (2011).
37. A. T. Ting, M. J. M. Bertrand, More to Life than NF-κB in TNFR1 Signaling. *Trends Immunol* **37**, 535–545 (2016).
38. P. Sharma, R. Varma, R. C. Sarasij, Ira, K. Gousset, G. Krishnamoorthy, M. Rao, S. Mayor, Nanoscale Organization of Multiple GPI-Anchored Proteins in Living Cell Membranes. *Cell* **116**, 577–589 (2004).
39. E. Sitarska, A. Diz-Muñoz, Pay attention to membrane tension: Mechanobiology of the cell surface. *Curr Opin Cell Biol* **66**, 11–18 (2020).
40. M. Simunovic, E. Evergren, I. Golushko, C. Prévost, H.-F. Renard, L. Johannes, H. T. McMahon, V. Lorman, G. A. Voth, P. Bassereau, How curvature-generating proteins build scaffolds on membrane nanotubes. *Proceedings of the National Academy of Sciences* **113**, 11226–11231 (2016).
41. M. Simunovic, G. A. Voth, Membrane tension controls the assembly of curvature-generating proteins. *Nat Commun* **6**, 7219 (2015).
42. A. Colom, E. Derivery, S. Soleimanpour, C. Tomba, M. D. Molin, N. Sakai, M. González-Gaitán, S. Matile, A. Roux, A fluorescent membrane tension probe. *Nat Chem* **10**, 1118–1125 (2018).
43. C. Roffay, G. Molinard, K. Kim, M. Urbanska, V. Andrade, V. Barbarasa, P. Nowak, V. Mercier, J. García-Calvo, S. Matile, R. Loewith, A. Echard, J. Guck, M. Lenz, A. Roux, Passive coupling of membrane tension and cell volume during active response of cells to osmosis. *Proc Natl Acad Sci U S A* **118** (2021).
44. A. Bhattacharya, M. Agarwal, R. Mukherjee, P. Sen, D. K. Sinha, 3D micro-environment regulates NF-κβ dependent adhesion to induce monocyte differentiation. *Cell Death Dis* **9**, 914 (2018).

45. G. Kustermans, J. El Benna, J. Piette, S. Legrand-Poels, Perturbation of actin dynamics induces NF-kappaB activation in myelomonocytic cells through an NADPH oxidase-dependent pathway. *Biochem J* **387**, 531–40 (2005).
46. M. Agarwal, P. Biswas, A. Bhattacharya, D. K. Sinha, Reactive oxygen species-mediated cytoplasmic stiffening impairs the phagocytic ability of the macrophage. *J Cell Sci* **133** (2020).
47. V. H. Guaiquil, J. C. Vera, D. W. Golde, Mechanism of Vitamin C Inhibition of Cell Death Induced by Oxidative Stress in Glutathione-depleted HL-60 Cells. *Journal of Biological Chemistry* **276**, 40955–40961 (2001).
48. R. W. Jackman, M. G. Rhoads, E. Cornwell, S. C. Kandarian, Microtubule-mediated NF-kappaB activation in the TNF-alpha signaling pathway. *Exp Cell Res* **315**, 3242–9 (2009).
49. D. F. Legler, O. Micheau, M.-A. Doucey, J. Tschopp, C. Bron, Recruitment of TNF Receptor 1 to Lipid Rafts Is Essential for TNFα-Mediated NF-κB Activation. *Immunity* **18**, 655–664 (2003).
50. B. Sinha, D. Köster, R. Ruez, P. Gonnord, M. Bastiani, D. Abankwa, R. V. Stan, G. Butler-Browne, B. Vedie, L. Johannes, N. Morone, R. G. Parton, G. Raposo, P. Sens, C. Lamaze, P. Nassoy, Cells Respond to Mechanical Stress by Rapid Disassembly of Caveolae. *Cell* **144**, 402–413 (2011).
51. S. R. Hubbard, W. T. Miller, Receptor tyrosine kinases: mechanisms of activation and signaling. *Curr Opin Cell Biol* **19**, 117–23 (2007).
52. N. C. Hartman, J. T. Groves, Signaling clusters in the cell membrane. *Curr Opin Cell Biol* **23**, 370–376 (2011).
53. A. Burt, C. K. Cassidy, P. Ames, M. Bacia-Verloop, M. Baulard, K. Huard, Z. Luthey-Schulten, A. Desfosses, P. J. Stansfeld, W. Margolin, J. S. Parkinson, I. Gutsche, Complete structure of the chemosensory array core signalling unit in an E. coli minicell strain. *Nat Commun* **11**, 743 (2020).
54. B. R. Caré, H. A. Soula, Impact of receptor clustering on ligand binding. *BMC Syst Biol* **5**, 48 (2011).
55. A. K. Lewis, C. C. Valley, J. N. Sachs, TNFR1 signaling is associated with backbone conformational changes of receptor dimers consistent with overactivation in the R92Q TRAPS mutant. *Biochemistry* **51**, 6545–6555 (2012).
56. G. H. Patterson, D. W. Piston, B. G. Barisas, Förster Distances between Green Fluorescent Protein Pairs. *Anal Biochem* **284**, 438–440 (2000).
57. H. Chakraborty, A. Chattopadhyay, Excitements and challenges in GPCR oligomerization: Molecular insight from FRET. *ACS Chem Neurosci* **6**, 199–206 (2015).
58. F. T. S. Chan, C. F. Kaminski, G. S. Kaminski Schierle, HomoFRET fluorescence anisotropy imaging as a tool to study molecular self-assembly in live cells. *Chemphyschem* **12**, 500–9 (2011).
59. C. H. Lo, E. C. Huber, J. N. Sachs, Conformational states of TNFR1 as a molecular switch for receptor function. *Protein Science* **29**, 1401–1415 (2020).
60. T. Mandal, A. Biswas, T. Ghosh, S. Manikandan, A. Kundu, A. Banerjee, D. Mitra, B. Sinha, Mechano-regulation by clathrin pit-formation and passive cholesterol-dependent tubules during de-adhesion. *Cell Mol Life Sci* **81**, 43 (2024).
61. A. Biswas, A. Alex, B. Sinha, Mapping Cell Membrane Fluctuations Reveals Their Active Regulation and Transient Heterogeneities. *Biophys J* **113**, 1768–1781 (2017).

Acknowledgments

We express our gratitude to the Central Scientific Services (CSS) of the Indian Association for the Cultivation of Science (IACS), Kolkata, for providing us with access to instrumental facilities. Special thanks to Mrs. Debapriya Ghatak, Mr. Chanchal Kumar Das, and Mr. Gopal Krishna Manna for their invaluable assistance with confocal microscopy, FACS, and graphical illustration, respectively. We are indebted to Prof. Maria Vartiainen (University of Helsinki, Finland) for generously gifting us with the GFP-GFP (2GFP) plasmid. Our appreciation goes to Dr. Dipyaman Ganguly (Indian Institute of Chemical Biology, Kolkata) for graciously allowing us to utilize FACS and to his student, Ms. Shreya Roy, for assisting with flow cytometry data acquisition. We also extend our gratitude to Dr. Prosenjit Sen (IACS, Kolkata) for providing us with an essential cell line (THP-1). BS thanks Wellcome Trust/DBT India Alliance fellowship (Grant Number IA/I/13/1/500885) for the TIRF imaging and the DBS-Builder Imaging facility (BT/INF/22/SP45383/2022) for their support with super-resolution STED imaging. We acknowledge ChatGPT 3.5 for rephrasing our write-up for clarity. Finally, we thank Dr. Mahesh Agarwal for critically reading the manuscript and providing valuable suggestions, which greatly contributed to preparing this manuscript for publication. Furthermore, we acknowledge IACS, Kolkata, for providing intramural funds.

Funding:

SERB Core Research Grant, Department of Science and Technology, Ministry of Science and Technology CRG/2022/005356 (DKS)

Department of Biotechnology, Ministry of Science and Technology BT/PR6995/BRB/10/1140/2012 (DKS)

SERB Grant number SERB_CRG_2458 (BS)

CEFIPRA Grant number 6303-1 (BS)

Indian Association for the Cultivation of Science, Kolkata 700032, India (SJ, PR, PB, NN)

Council of Scientific and Industrial Research (PR)

University Grants Commission (JD)

Author contributions: SJ and PR are co-first authors of this paper and contributed equally. DKS, BS, SJ, and PR designed the project and prepared the manuscript. SJ, PR, and JD conducted the experiments and analyzed the data. JD performed the IRM, TIRF and, STED imaging. PB was

responsible for setting up and calibrating the HeLa-mEGFP and HeLa-2GFP fluorescence anisotropy (r) measurements. NN contributed to data analysis. BS analyzed the STED data and assisted in reviewing the manuscript.

Competing interests: The authors declare that they have no competing interests.

Data and materials availability: All data are available in the main text or the supplementary materials. Codes used in the manuscript are freely available online (https:/github.com/SubhamoyJana/TNFR1-Project).

Figures

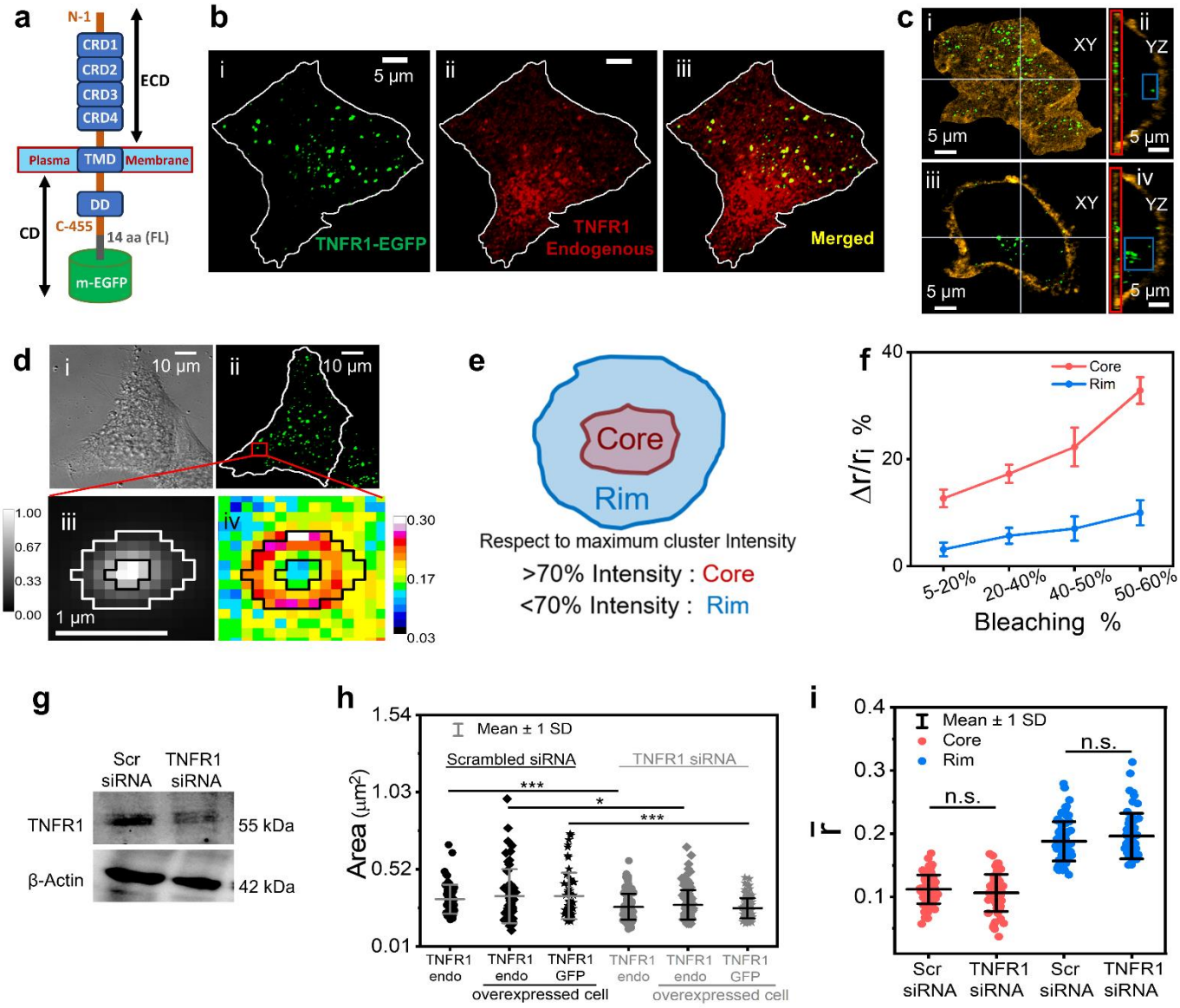

Fig. 1. Homo-FRET efficiency of TNFR1-EGFP reveals IRD map.

(a) Schematic representation of TNFR1-EGFP protein depicts ECD: extracellular domain, CRD: cysteine-rich domain, TMD: transmembrane domain, CD: cytoplasmic domain, DD: death domain, FL: flexible linker. **(b)** Representative confocal image of HeLa cell transfected with TNFR1-EGFP (i, green) immunostained with anti-TNFR1 antibody (ii, red). Overlay of TNFR1-EGFP and anti-TNFR1 is shown in iii. **(c)** XY and YZ sections of 3D confocal images of HeLa cells expressing TNFR1-EGFP (green), stained with CellMask Orange (orange) to label the plasma membrane. The basal (z=0; i and ii) and the mid plane (z=10; iii and iv) sections of the cell indicate the localization of clusters on the

plasma membrane or in the cytoplasm. ii and iv represent the YZ cross-sections of i and iii, respectively. The red box encloses clusters on the plasma membrane, while the blue box encompasses clusters in the cytoplasm. **(d)** Representative DIC (i) and fluorescence (ii) images of a HeLa cell expressing TNFR1-EGFP; zoomed in image of a single cluster showing its (iii) intensity and (iv) fluorescence anisotropy map. **(e)** Schematic diagram of an individual cluster showing two different compactional regimes (core and rim). **(f)** Percentage change in relative mean fluorescence anisotropy ($\Delta r = \bar{r}_f - \bar{r}_i$ where $\bar{r}_f$ is the corresponding mean anisotropy after photo-bleaching and $\bar{r}_i$ is the pre-bleach mean anisotropy) of core (red) and rim (blue) regions of TNFR1-EGFP clusters with the percentage of photobleaching in live HeLa cells. Data are presented as means ± SEM of n=20 clusters in 3 cells each in two independent experiments. **(g)** The expression of TNFR1 and β-Actin in HeLa cells transfected with TNFR1-siRNA (as compared to scrambled siRNA) was analyzed using immunoblotting. Immunoblot is representative of two independent experiments. **(h)** Quantification of cluster area (μm^2) of endogenous TNFR1 clusters (n=100) in non-transfected and, TNFR1-EGFP transfected cells. Quantification of cluster area of TNFR1-EGFP (exogeneous) clusters (n=100) in HeLa cells transfected with scrambled siRNA (black) and TNFR1 siRNA (grey), respectively. Data are representative of 3 cells each in three independent experiments. **(i)** Mean fluorescence anisotropy ($\bar{r}$) of core (red) and rim (blue) regions of TNFR1-EGFP clusters (n=60) in HeLa cells transfected with scrambled siRNA and TNFR1 siRNA, respectively. Data are representative of 3 cells each in three independent experiments. Significance between data sets was determined by two-tailed Student's t-test **(h, i)** and is indicated in the figures as follows: $*P < 0.05$; $**P < 0.01$; $***P < 0.001$; n.s., not significant. Scale bars are indicated in corresponding images.

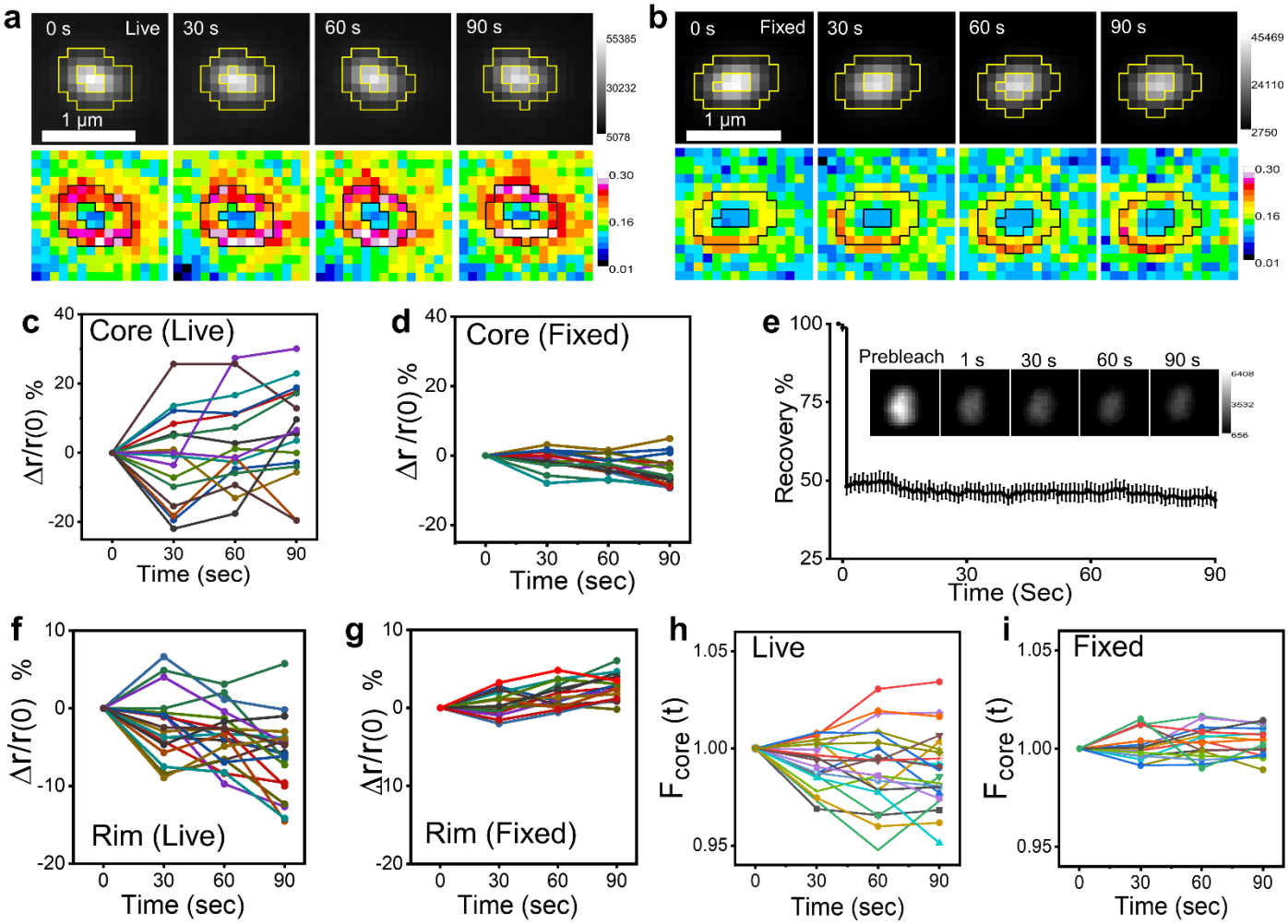

Fig. 2. Intra-cluster spatiotemporal dynamics of TNFR1-EGFP.

(a, b) Time-lapse intensity (upper panel) and anisotropy maps (lower panel) of a single TNFR1-EGFP cluster in live and fixed HeLa cells, respectively. **(c, d)** Percentage change in relative mean fluorescence anisotropy $\frac{\Delta r}{\bar{r}(0)}$, where $\Delta r = \bar{r}(t) - \bar{r}(0)$ of the core region with time t in live and fixed HeLa cells, respectively. Here $\bar{r}(t)$ represents the mean anisotropy at time t. **(e)** Fluorescence recovery of TNFR1-EGFP clusters after photobleaching up to 90 seconds with 1-second interval measured by confocal microscopy. Data are presented as means ± SEM of n=10 clusters in 2 cells. Confocal microscopy image of a representative TNFR1-EGFP cluster before and after photobleaching is given in inset. **(f, g)** Percentage change in relative mean fluorescence anisotropy $\frac{\Delta r}{\bar{r}(0)}$ of the rim region with time t in live and fixed HeLa cells, respectively. **(h, i)** Change in fractional fluorescence intensity $\left(F_{core}(t) = \right.$

$\left(\frac{\frac{\bar{I}_{core}(t)}{(\bar{I}_{core}(t)+\bar{I}_{rim}(t))}}{\frac{\bar{I}_{core}(0)}{(\bar{I}_{core}(0)+\bar{I}_{rim}(0))}}\right)$ of the core region of TNFR1-EGFP clusters with time t in live and fixed HeLa cells, respectively. Here $\bar{I}_{core}(t)$ and $\bar{I}_{rim}(t)$represent the mean fluorescence intensity in the core and the rim at time t. Data are representative of n=20 clusters in 2 cells each in two independent experiments **(c, d, f, g, h, i).** Scale bars are indicated in corresponding images.

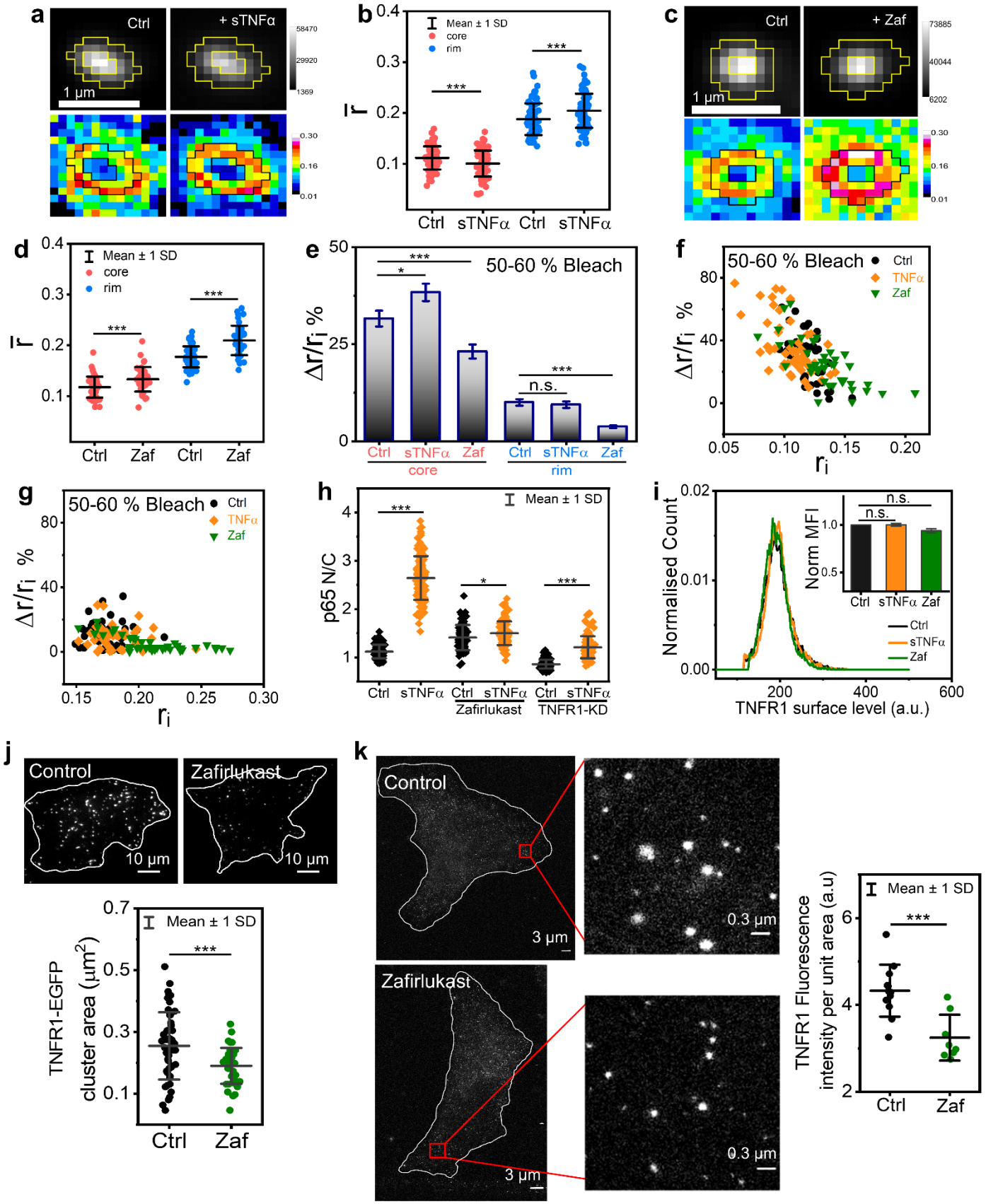
a
Ctrl
+ sTNFα
1 µm
58470
29920
1369
0.30
0.16
0.01
b
Mean ± 1 SD
core
rim
r
Ctrl
sTNFα
Ctrl
sTNFα
c
Ctrl
+ Zaf
1 µm
73885
40044
6202
d
Mean ± 1 SD
core
rim
r
Ctrl
Zaf
Ctrl
Zaf
e
50-60 % Bleach
Δr/ri %
Ctrl
sTNFα
Zaf
Ctrl
sTNFα
Zaf
core
rim
n.s.
f
50-60 % Bleach
Ctrl
TNFα
Zaf
Δr/ri %
ri
g
50-60 % Bleach
Ctrl
TNFα
Zaf
Δr/ri %
ri
h
Mean ± 1 SD
p65 N/C
Ctrl
sTNFα
Ctrl
sTNFα
Ctrl
sTNFα
Zafirlukast
TNFR1-KD
i
Normalised Count
TNFR1 surface level (a.u.)
Norm MFI
n.s.
n.s.
Ctrl
sTNFα
Zaf
j
Control
Zafirlukast
10 µm
10 µm
Mean ± 1 SD
TNFR1-EGFP cluster area (µm²)
Ctrl
Zaf
k
Control
Zafirlukast
3 µm
0.3 µm
TNFR1 Fluorescence intensity per unit area (a.u)
Mean ± 1 SD
Ctrl
Zaf

926

Fig. 3. IRD modulates downstream signal activation of TNFR1.

(a) Representative fluorescence images (upper panel) of the same TNFR1-EGFP cluster and the corresponding anisotropy (r) maps (lower panel) before (Ctrl) and after sTNF-α treatment (20 ng/mL, 5 minutes). **(b)** Mean fluorescence anisotropy ($\bar{r}$) of core (red) and rim (blue) regions of TNFR1-EGFP clusters with and without sTNF-α addition. Data are representative of n=90 clusters in 5 cells each in three independent experiments. **(c)** Representative fluorescence images (upper panel) of a TNFR1-EGFP cluster and the corresponding anisotropy (r) maps (lower panel) before (Ctrl) and after zafirlukast treatment (100 µM, 1 hour). **(d)** Mean fluorescence anisotropy ($\bar{r}$) of core (red) and rim (blue) regions of TNFR1-EGFP clusters with and without zafirlukast addition. Data are representative of n=90 clusters in 5 cells each in three independent experiments. **(e)** Percentage change in relative mean fluorescence anisotropy ($\Delta r = \bar{r}_f - \bar{r}_i$ where $\bar{r}_f$ is the corresponding mean anisotropy after photobleaching and $\bar{r}_i$ is the pre-bleach mean anisotropy) of core (red) and rim (blue) regions of TNFR1-EGFP clusters upon 50-60% photobleaching in control, sTNF-α and zafirlukast-treated HeLa cells. **(f, g)** Scatter plot of percentage change in relative mean anisotropy ($\Delta r = \bar{r}_f - \bar{r}_i$) with respect to initial mean anisotropy ($\bar{r}_i$) in core **(f)** and rim **(g)** regions upon 50-60% photobleaching in control, sTNF-α and zafirlukast-treated conditions, respectively. Data are representative of n=30 clusters in 2 cells each in three independent experiments **(e, f, g)**. **(h)** Nuclear to cytoplasmic (N/C) mean intensity ratio of endogenous NF-κB (p65) analyzed by immunostaining in HeLa cells (Ctrl) and HeLa cells treated with sTNF-α (20 ng/mL, 30 minutes) in Ctrl, zafirlukast-treated (100 µM, 1 hour) and TNFR1 siRNA (TNFR1-KD) conditions. The control groups (Ctrl) for each treatment are different, as shown in the figure. Data are representative of 35 cells each in three independent experiments. **(i)** Surface level expression of endogenous TNFR1 in control, sTNF-α (20 ng/mL, 30 minutes) and zafirlukast-treated (100 µM, 1 hour) HeLa cells as measured by flow cytometry. The mean fluorescence intensity (MFI) of each of them normalized with respect to control is shown in the inset. **(j)** Representative TIRF images of TNFR1-EGFP overexpressed control HeLa cells (upper panel, left) subjected to zafirlukast treatment (100 µM, 1 hour) (upper panel, right). Quantification of TNFR1-EGFP cluster area (µm^2) by TIRF (lower panel) before (n=49 clusters) and after (n=43 clusters) zafirlukast treatment. Data are presented as means ± SD of 2 cells each in three independent experiments. **(k)** Representative STED images of endogenous TNFR1 in control HeLa cells (upper panel) and zafirlukast-treated cells (lower panel), with their respective magnified regions of interest (marked in red box). Quantification of TNFR1

fluorescence intensity per unit area (a.u.) as estimated from STED images (n=12 cells for control and n=8 cells for zafirlukast-treated condition. For each cell, 6 ROIs were sampled. The number of clusters used were >150 per cell. Significance between data sets was determined by two-tailed Student's t-test **(b, d, e, h, i, j, k)** and is indicated in the figures as follows: $*P < 0.05$; $**P < 0.01$; $***P < 0.001$; n.s., not significant. Scale bars are indicated in corresponding images.

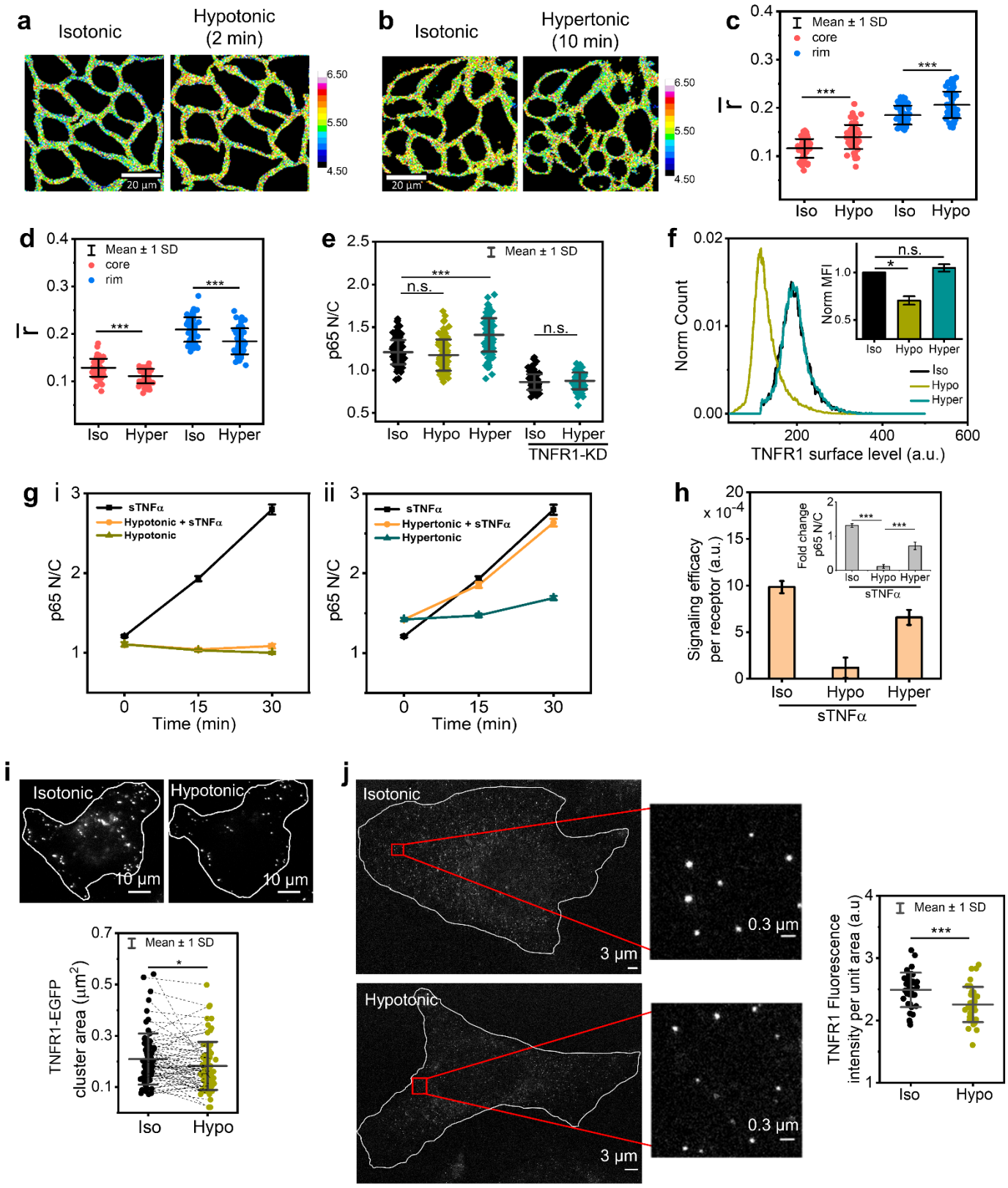

Fig. 4. Membrane tension regulates TNFR1 IRD and affects signaling efficacy.

(a, b) Fluorescence lifetime map of Flipper-TR (200 nM, 15 minutes) upon hypotonic (75% water, 2 minutes) and hypertonic (150 mM mannitol, 10 minutes) shock with respect to isotonic condition

respectively. Images are representative of 5 cells each in two independent experiments. **(c)** Mean fluorescence anisotropy ($\bar{r}$) of core (red) and rim (blue) regions of TNFR1-EGFP clusters upon hypotonic shock (75% water, 2 minutes) with respect to isotonic conditions. Data are representative of n=60 clusters in 5 cells each in three independent experiments. **(d)** Mean fluorescence anisotropy ($\bar{r}$) of core (red) and rim (blue) regions of TNFR1-EGFP clusters upon hypertonic shock (150 mM mannitol, 10 minutes) with respect to isotonic condition. Data are representative of n=60 clusters in 5 cells each in three independent experiments. **(e)** Nuclear to cytoplasmic (N/C) mean intensity ratio of endogenous NF-κB (p65) analyzed by immunostaining in HeLa cells subjected to hypotonic (75% water, 2 minutes) and hypertonic shock (150 mM mannitol, 10 minutes) with respect to isotonic condition in control and TNFR1-knockdown (TNFR1-KD) cells. Data are representative of 35 cells each in three independent experiments. **(f)** Surface level expression of endogenous TNFR1 of HeLa cells in isotonic, hypotonic (75% water, 2 minutes), and hypertonic conditions (150 mM mannitol, 10 minutes) as measured by flow cytometry. The mean fluorescence intensity (MFI) of each of them normalized with respect to isotonic condition is shown in the inset. **(g)** Quantification of p65 N/C ratio with time in (i) hypotonic and (ii) hypertonic conditions in response to sTNF-α with respect to isotonic condition. **(h)** p65 signaling efficacy of TNFR1 in HeLa cells subjected to isotonic, hypotonic, and hypertonic shocks in response to sTNF-α. The signaling efficacy denotes the changes in N/C ratio of p65 normalized with the respective levels of surface receptors (changes in N/C ratio of p65 / respective mean fluorescence intensities (MFI) of surface level TNFR1). The fold change of N/C ratio of p65 in HeLa cells subjected to isotonic, hypotonic, and hypertonic shocks in response to sTNF-α normalized by their respective basal levels (without sTNF-α), is given in inset. Data are representative of means ± SD of 30 cells each in three independent experiments. **(i)** Representative TIRF images of TNFR1-EGFP overexpressed control HeLa cells (upper panel, left) subjected to hypotonic shock within 2 minutes (upper panel, right). Quantification of TNFR1-EGFP cluster area (μm^2) of the same clusters (n=73) before and after hypotonic shock. Data are representative of means ± SD of 3 cells each in three independent experiments. **(j)** Representative STED images of endogenous TNFR1 in HeLa cells in isotonic (upper panel) and hypotonic (lower panel) conditions, with their respective magnified regions of interest (marked in red box). Quantification of TNFR1 fluorescence intensity per unit area (a.u.) as estimated from STED images (n=37 cells for isotonic and n=38 cells for hypotonic condition). Data are presented as means ± SD of 37/38 cells each in two independent experiments involving 6 ROIs per cell and

measurement of density for >700 clusters per cell. Significance between data sets was determined by two-tailed Student's t-test **(c, d, e, f, h, i, j)** and is indicated in the figures as follows: $*P < 0.05$; $**P < 0.01$; $***P < 0.001$; n.s., not significant. Scale bars are indicated in corresponding images.

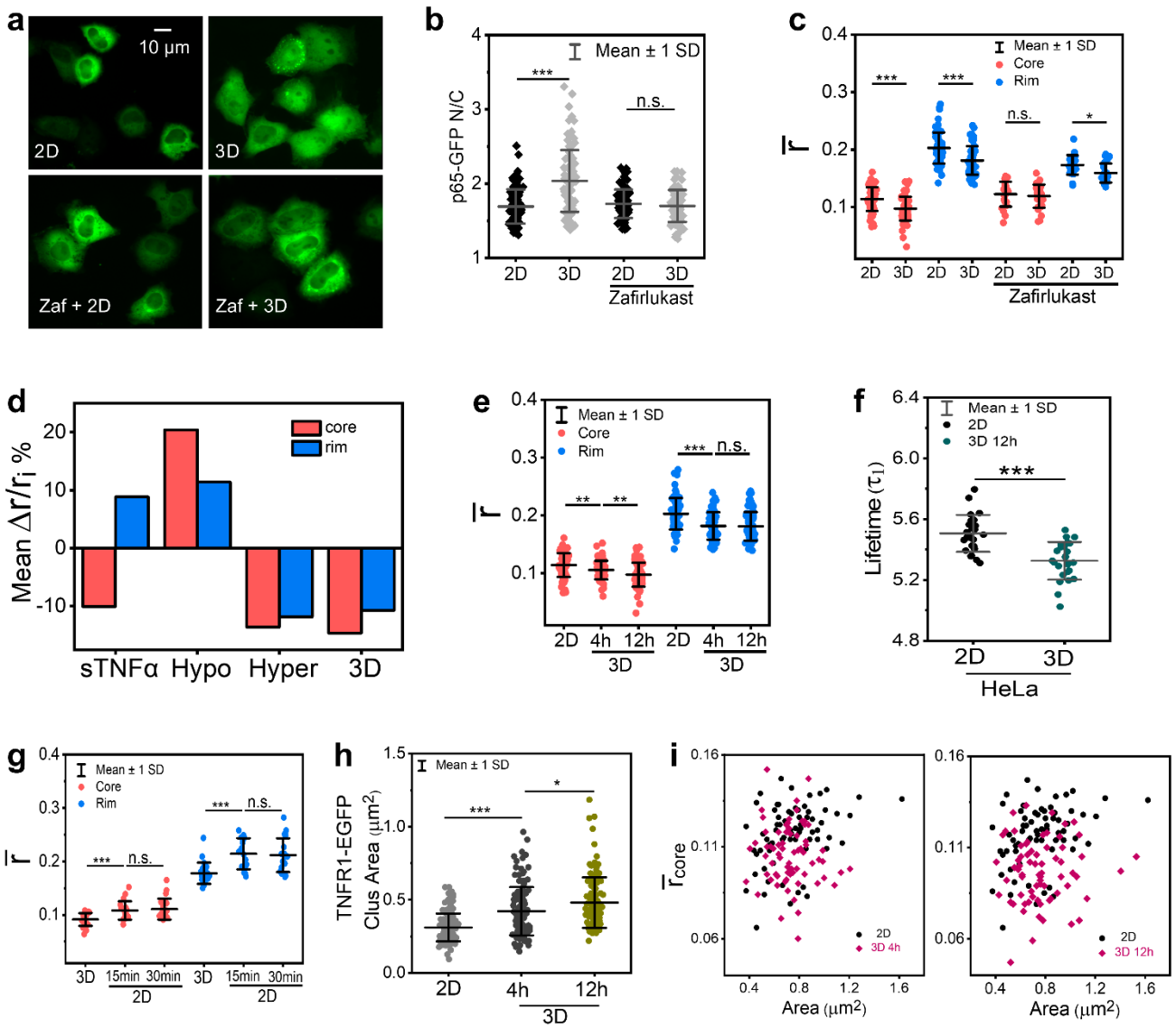

Fig. 5. 3D gel-like microenvironment triggers ligand-independent TNFR1 signaling in HeLa cells. **(a)** Live HeLa cells transfected with NF-κB-GFP (p65-GFP) in 2D (control) and 3D (1% agarose gel cover, 12 hours) in untreated and zafirlukast-treated conditions. **(b)** Nuclear to cytoplasmic (N/C) mean intensity ratio of p65-GFP in live HeLa cells in 2D (control) and 3D (1% agarose gel cover, 12 hours) in untreated and zafirlukast-treated conditions. Data are representative of 35 cells each in three independent experiments. **(c)** Mean fluorescence anisotropy ($\bar{r}$) of core (red) and rim (blue) regions of TNFR1-EGFP clusters in HeLa cells in 2D (control) and 3D (1% agarose gel cover, 12 hours) in untreated and zafirlukast-treated conditions. Data are representative of n=60 clusters in 3 cells each in three independent experiments. **(d)** Percentage change in relative mean fluorescence anisotropy (Δr) of core (red) and rim (blue) regions of TNFR1-EGFP clusters in HeLa cells in sTNF-α-treated, hypotonic, hypertonic, and 3D conditions, normalized with their respective controls. Data are representative of

n=60 clusters in 3 cells each in three independent experiments. **(e)** Mean fluorescence anisotropy ($\bar{r}$) of core (red) and rim (blue) regions of TNFR1-EGFP clusters in HeLa cells transitioning from 2D (control) to 3D (1% agarose gel cover) after 4 hours and 12 hours of incubation. Data are representative of n=60 clusters in 3 cells each in three independent experiments. **(f)** Fluorescence lifetime (τ_1) of Flipper-TR of HeLa cells in 2D (control) and 3D (1% agarose gel cover, 12 hours). Data are representative of 5 cells each in three independent experiments. **(g)** Mean fluorescence anisotropy ($\bar{r}$) of core (red) and rim (blue) regions of TNFR1-EGFP in HeLa cells transitioning from 3D (1% agarose gel cover) to 2D (control) after 15 minutes and 30 minutes of incubation. Data are representative of n=20 clusters in 2 cells each in two independent experiments. **(h)** Quantification of TNFR1-EGFP cluster area (μm^2) in HeLa cells in 2D (control) and 3D (1% agarose gel cover) after 4 hours and 12 hours of incubation. Data are representative of n=124 clusters in 5 cells each in three independent experiments. **(i)** Scatter plot of TNFR1-EGFP cluster area (μm^2) vs fluorescence anisotropy of core ($\bar{r}_{core}$) in HeLa cells in 2D (control) and 3D (1% agarose gel cover) after 4 hours (left) and 12 hours (right) of incubation. Data are representative of 3 cells each in three independent experiments (n=70 clusters). Significance between data sets was determined by two-tailed Student's t-test **(b, c, e, f, g, h)** and is indicated in the figures as follows: $*P < 0.05$; $**P < 0.01$; $***P < 0.001$; n.s., not significant. Scale bars are indicated in corresponding images.

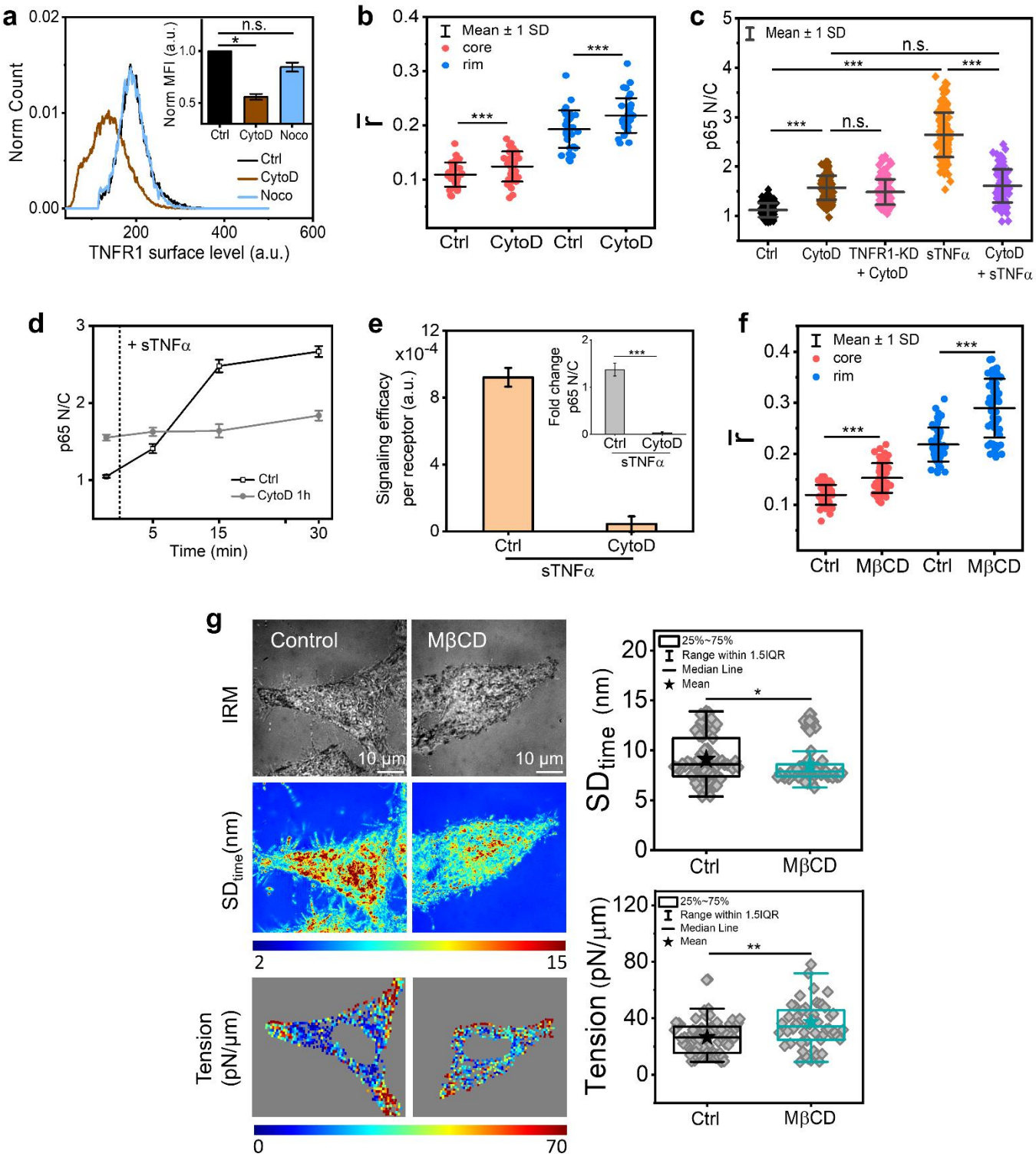

Fig. 6. Disassembly of F-actin and cholesterol depletion reduces sTNF-α-mediated TNFR1 signaling efficacy by altering TNFR1 IRD.

(a) Surface level expression of endogenous TNFR1 of HeLa cells treated with cytochalasin D (2 μM, 1 hour) and nocodazole (18 μM, 2 hours) along with control, as measured by flow cytometry. The mean

fluorescence intensity (MFI) of each of them normalized with respect to control is shown in the inset. **(b)** Mean fluorescence anisotropy ($\bar{r}$) of core (red) and rim (blue) regions of TNFR1-EGFP clusters in HeLa cells in control and cytochalasin D-treated conditions. Data are representative of n=60 clusters in 3 cells each in three independent experiments. **(c)** Nuclear to cytoplasmic (N/C) mean intensity ratio of NF-κB (p65) analyzed by immunostaining in control, cytochalasin D-treated condition in control and TNFR1-knockdown (TNFR1-KD) HeLa cells, and sTNF-α-treated condition in control and cytochalasin D-treated HeLa cells. Data are representative of 35 cells each in three independent experiments. **(d)** Change in N/C ratio of endogenous p65 with time in HeLa cells in control and cytochalasin D-treated conditions. Data are presented as means ± SEM of 35 cells each in three independent experiments. **(e)** p65 signaling efficacy of TNFR1 in control and cytochalasin D-treated HeLa cells in response to sTNF-α. The signaling efficacy denotes the changes in N/C ratio of p65 normalized with the respective levels of surface receptors (changes in N/C ratio of p65 / respective mean fluorescence intensities (MFI) of surface level TNFR1). The fold change of N/C ratio of p65 in in control and cytochalasin D-treated HeLa cells in response to sTNF-α normalized by their respective basal levels (without sTNF-α), is given in inset. Data are representative of means ± SD of 30 cells each in three independent experiments. **(f)** Mean fluorescence anisotropy ($\bar{r}$) of core (red) and rim (blue) regions of TNFR1-EGFP clusters in HeLa cells in control and MβCD-treated (2 mM, 1 hour) conditions. Data are representative of n=60 clusters in 3 cells each in three independent experiments. **(g)** Representative IRM (Interference Reflection Microscopy) images (upper panel), corresponding SD_{time} maps (middle panel) and membrane tension maps (lower panel) of control and MβCD-treated (2 mM, 1 hour) HeLa cells. Comparison of SD_{time} (nm) of membrane fluctuation (upper right panel) and membrane tension (pN/μm) (lower right panel) in control (n=79 cells) and MβCD-treated (n=57 cells) cells. Data are representative of three independent experiments. Significance between data sets was determined by two-tailed Student's t-test **(a, b, c, e, f, g)** and is indicated in the figures as follows: $*P < 0.05$; $**P < 0.01$; $***P < 0.001$; n.s., not significant. Scale bars are indicated in corresponding images.

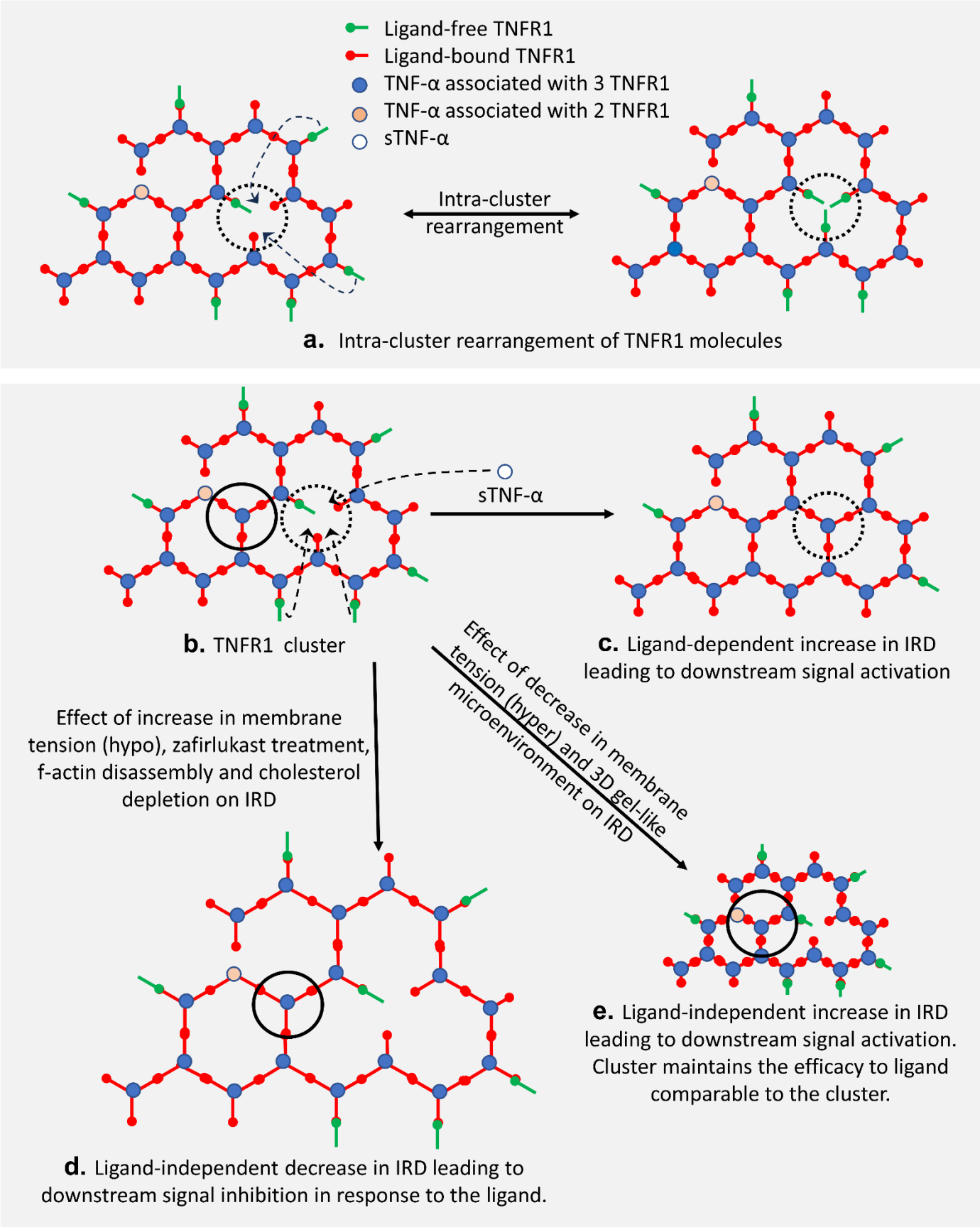
Ligand-free TNFR1
Ligand-bound TNFR1
TNF-α associated with 3 TNFR1
TNF-α associated with 2 TNFR1
sTNF-α
Intra-cluster rearrangement
a. Intra-cluster rearrangement of TNFR1 molecules
sTNF-α
b. TNFR1 cluster
c. Ligand-dependent increase in IRD leading to downstream signal activation
Effect of decrease in membrane tension (hyper) and 3D gel-like microenvironment on IRD
Effect of increase in membrane tension (hypo), zafirlukast treatment, f-actin disassembly and cholesterol depletion on IRD
e. Ligand-independent increase in IRD leading to downstream signal activation. Cluster maintains the efficacy to ligand comparable to the cluster.
d. Ligand-independent decrease in IRD leading to downstream signal inhibition in response to the ligand.

Fig. 7. Schematic representation of IRD dynamics in TNFR1 clusters (top view).

(a) Spontaneous rearrangement of TNFR1 molecules within clusters, showing two possible states. The vacant site for ligand is enclosed by a black dotted circle, which can be occupied by ligand-free TNFR1 molecules (green) in the rim as indicated by the dashed arrows. Both the black dotted circles have same area indicating the changes in IRD due to intra-cluster reorganization of TNFR1. **(b)** The depicted TNFR1 cluster includes a vacant site for ligand (indicated by a black dotted circle), with 3 ligand-bound TNFR1 molecules (red) and 1 ligand-free TNFR1 molecule (green). Additionally, the black solid circle represents a different region of the cluster where 6 TNFR1 molecules are in a ligand-bound state (red). **(c)** Following the addition of the ligand sTNF-α, reorganization of TNFR1 molecules occurs. The ligand binds to the vacant site (indicated by a black dotted circle), leading to the reshuffling of free TNFR1 molecules (green) located at the periphery of the cluster (dashed arrow). This process results in an increase in the number of receptors (IRD) within the black dotted circle, reaching up to 6 ligand-bound TNFR1 molecules (red). **(d)** Elevation in membrane tension (hypotonic shock), zafirlukast treatment, disruption of F-actin, and depletion of cholesterol lead to a decrease in TNFR1 IRD. This is illustrated by an increase in TNFR1 inter-molecular distances within the cluster, as indicated by the black solid circle, in comparison to the TNFR1 cluster (b). The black solid circles of equal area in (b) and (d) suggest that the number of receptors (IRD) in the circle decreases to less than 6 compared to (b). This reduction in IRD hinders downstream signaling in response to sTNF-α. **(e)** A decrease in membrane tension (caused by hypertonic shock) and the presence of a 3D gel-like microenvironment both lead to an increase in the TNFR1 IRD. This increase is depicted by a decrease in TNFR1 inter-molecular distances (illustrated by a black solid circle) within the cluster compared to the TNFR1 cluster (b). The black solid circles of equal area in (b) and (e) suggest that the number of receptors (IRD) in the circle increases to more than 6 compared to (b). This increase in IRD facilitates ligand-independent downstream signaling.